

Article

Early Ediacaran Magmatism in the Yenisei Ridge and Evolution of the Southwestern Margin of the Siberian Craton

Antonina Vernikovskaya ^{1,2,*}, Valery A. Vernikovskiy ^{1,2}, Nikolay Matushkin ^{1,2} , Pavel Kadilnikov ^{1,2}, Dmitry V. Metelkin ^{1,2}, Irina Romanova ¹, Zheng-Xiang Li ³ and Egor Bogdanov ^{1,2}

¹ A.A. Trofimuk Institute of Petroleum Geology and Geophysics, Siberian Branch of the Russian Academy of Sciences, prosp. Akad. Koptiyuga, 3, 630090 Novosibirsk, Russia; VernikovskiyVA@ipgg.sbras.ru (V.A.V.); matushkinny@ipgg.sbras.ru (N.M.); kadilnikovpi@ipgg.sbras.ru (P.K.); MetelkinDV@ipgg.sbras.ru (D.V.M.); romanovaiv@ipgg.sbras.ru (I.R.); bogdanovea@ipgg.sbras.ru (E.B.)

² Department of Geology and Geophysics, Novosibirsk State University, ul. Pirogova, 1, 630090 Novosibirsk, Russia

³ Earth Dynamics Research Group, ARC Centre of Excellence for Core to Crust Fluid systems (CCFS) and The Institute for Geoscience Research (TIGeR), School of Earth and Planetary Sciences, Curtin University, GPO Box U1987, 6845 Perth, Australia; Z.Li@exchange.curtin.edu.au

* Correspondence: vernikovskayaae@ipgg.sbras.ru

Received: 29 May 2020; Accepted: 21 June 2020; Published: 23 June 2020



Abstract: We present the first comprehensive data for the early Ediacaran stage of evolution of the western active continental margin of the Siberian Craton (Yenisei Ridge). U-Pb (SHRIMP-II SIMS) data for zircons from dikes of picrodolerites, quartz diorites, and leucocratic granites show that they were emplaced at 625 ± 5 , 623 ± 8 , and 626 ± 5 Ma, respectively, which indicates a narrow time window of Ediacaran magmatic events. The mafic tholeiitic rocks have OIB and E-MORB mantle components in their magmatic sources. Mineralogical and geochemical observations showed that the mantle-sourced mafic melts assimilated some crustal material, forming Th-enriched dikes of intermediate composition and K- and Rb-enriched felsic rocks. The possible geodynamic conditions for the formation of these early Ediacaran dikes are shown and a geodynamic model is presented for the development of the Yenisei Ridge orogen from the late Cryogenian to the late Ediacaran.

Keywords: Siberian Craton; Yenisei Ridge; dikes; magmatism; U-Pb and Ar-Ar geochronology; continental margin; Ediacaran

1. Introduction

The Ediacaran is one of the key evolution stages for fold belts surrounding the Siberian Craton from the north, west, and south. It is in this period that strong tectonic transformations caused by accretionary-collisional events manifested on the Taimyr Peninsula, in the Eastern Sayan and the Transbaikalia Region [1–5]. As became clear in recent years, the Ediacaran stage was one of the main periods in the tectonic evolution of the Yenisei Ridge—A key structure in the western margin of the Siberian Craton [6], whose accretionary-collisional structure still needs to be further investigated. In addition, the Neoproterozoic–Paleozoic accretionary processes on the western margin of Siberia represent the early stages of formation of the Central Asian Orogenic Belt that are still not fully clear. The area adjacent to the western border of the Yenisei Ridge serves as the basement for the Fore-Yenisei sedimentary basin [7], which is essential for understanding the relationships between the platform cover and the folded margin of the Siberian paleocontinent in this time interval.

Previous studies established the features of the tectonic evolution of the Yenisei Ridge orogen in the pre-Ediacaran time—From the transformation of the passive continental margin of the Siberian craton in an active one in the Tonian at ~800 Ma, when the Central Angara terrane collided with the Siberian Craton and caused the formation of syncollisional (760–750 Ma) and postcollisional (750–720 Ma) granites [4,6,8,9]. Then from the early Cryogenian to the early Ediacaran (711–628 Ma), a subduction zone evolved along the western margin of Siberia. This led to the synchronous formation of island arcs, which subsequently accreted to the continent, and an active continental margin complex that formed on the Craton in the back-arc position [10–13]. Unlike the Tonian and Cryogenian-early Ediacaran magmatic events that are well recorded in collisional granites and suprasubductional rocks, the middle Ediacaran magmatism on the Yenisei Ridge was less pronounced and so was less studied. The only formation that was identified indicating the evolution of the subduction system is a late Ediacaran adakite-gabbro-anorthosite association (576–546 Ma) in the South Yenisei Ridge [14].

Therefore, in this study we present new data on the early Ediacaran magmatic stage in the evolution of the western margin of Siberia within the Yenisei Ridge on the example of dike complexes. We aim to determine the geodynamic formation setting of these dike complexes, which will help to complement our tectonic reconstruction of the whole Yenisei Ridge orogen. The origin of Neoproterozoic dikes and associating igneous rocks in the fold belts of the margins of the Siberian Craton is a debatable topic. These magmatic complexes were considered in connection to various geodynamic settings, such as continental rifting during the breakup of the Rodinia supercontinent [15,16], or an active continental margin of Siberia [10,14,17–21] on the early formation stages of the Central Asian fold belt. To solve these discussions, we will give particular attention to the nature, composition, and age of the Neoproterozoic mafic, intermediate, and felsic dikes.

2. Geological Setting

Our studies were performed in the southern part of the Yenisei Ridge in the junction zone of the Tatarka-Ishimba and Yenisei sutures along 150–160 km of outcrops along the banks of the Yenisei River (Figures 1 and 2).

The mafic rocks from dikes (picrodolerites and dolerites) were studied in the east bank of Yenisei River, 12–20 km upstream of the Angara River mouth. They form a group of 20 bodies with thicknesses up to 3 m (Figures 2 and 3c). Host rocks in this locality are deformed deposits of the Gorevka Formation composed of limestones, calc-argillaceous shales, and calcareous sandstones (NP₁₋₂) [22]. The 718-Ma (U-Pb age) Strelka pluton granites intrude the sedimentary succession, and thus represent the minimal age for this unit [23]. The carbonate rocks are folded with steeply dipping (80°) axial planes towards the west-northwest (285°–308°) or the west-southwest (247–260°). These dikes are spatially associated with the axial planes of the folds. Individual dikes and host limestones are in some places cut by low amplitude (<1 m) reverse faults and shallow thrusts with up to 5 m displacement, with fault planes dipping to the west–northeast.

The intermediate and felsic dikes (quartz diorites and leucocratic granites) in the region were studied on the left bank of the Yenisei River, 2 km upstream of the Abeyka River mouth and 2.5 km upstream of the Yarlychikha River mouth, respectively (Figures 2 and 3a,b). The dikes are non-deformed and intrude Neoproterozoic (Cryogenian–Ediacaran) rocks of the Predivinsk terrane: Island arc metagabbroids of the Yarlychikha pluton and metavolcanics associated with plagiogranites of the Yagunov pluton. The volcanogenic sequence of calc-alkaline series is composed of calc-alkaline basalts, basaltic andesites, dacites, rhyodacites, rhyolites, as well as acidic and mafic tuffs (Figure 2b). Results of U-Pb dating of zircons for metarhyolites and plagiogranites placed their formation at 637 ± 5 and 628 ± 3 Ma, respectively [10,11]. The main deformations in these host rocks have a northeastern vergence, showing accretion and obduction processes of attachment of the island arc blocks to the Siberian Craton margin [24]. That is to say, the host rocks, which have a foliation (S₁) dipping to 226–235° at angles of 72–77° and 234–235° at angles 35–50°, are cut by faults deformed into folds with axial planes dipping to the east-southeast (95–103°) at angles 10–80°. Later strike-slip-related deformations

manifest as superimposed west-dipping smaller folds and south-dipping hinges (173–185°, angles 37–65°) that are oriented at an angle close to 45° to the S₁ foliation strike. In addition, in the northeastern part of the Yarlychikha pluton there is a north-northeastern dipping banding in the metagabbroids with kinematic indicators showing sinistral (left-lateral) strike-slip displacements.

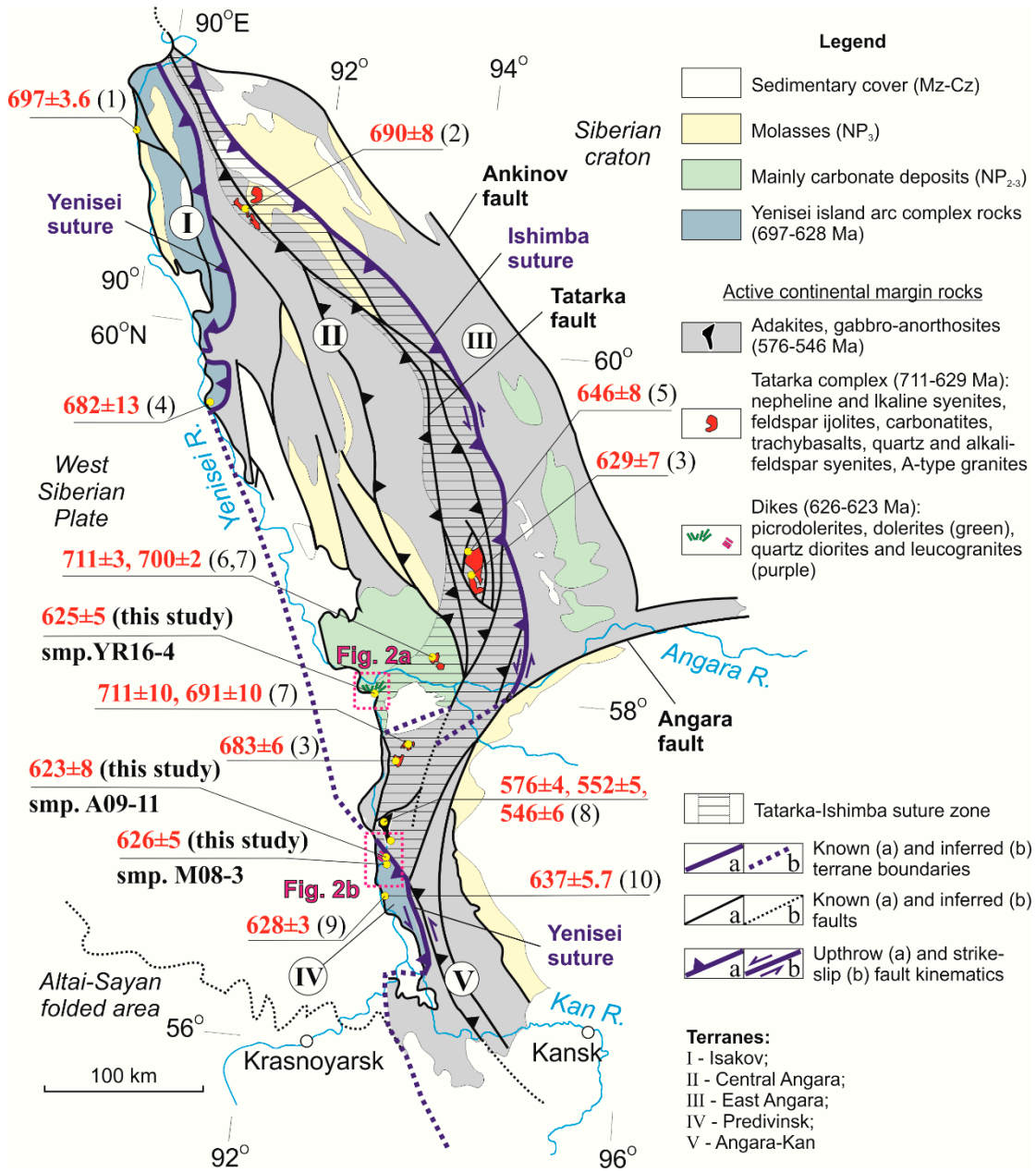


Figure 1. Tectonic scheme of the Yenisei Ridge showing localization and age of manifestations of Ediacaran and Cryogenian igneous rocks, modified after [10,22,24]. Red numbers show ages determined by U-Pb method. Numbers in brackets—reference sources: (1)—[12]; (2)—[16]; (3)—[9,25]; (4)—[13]; (5)—[21]; (6)—[18]; (7)—[26]; (8)—[14]; (9)—[10]; (10)—[11].

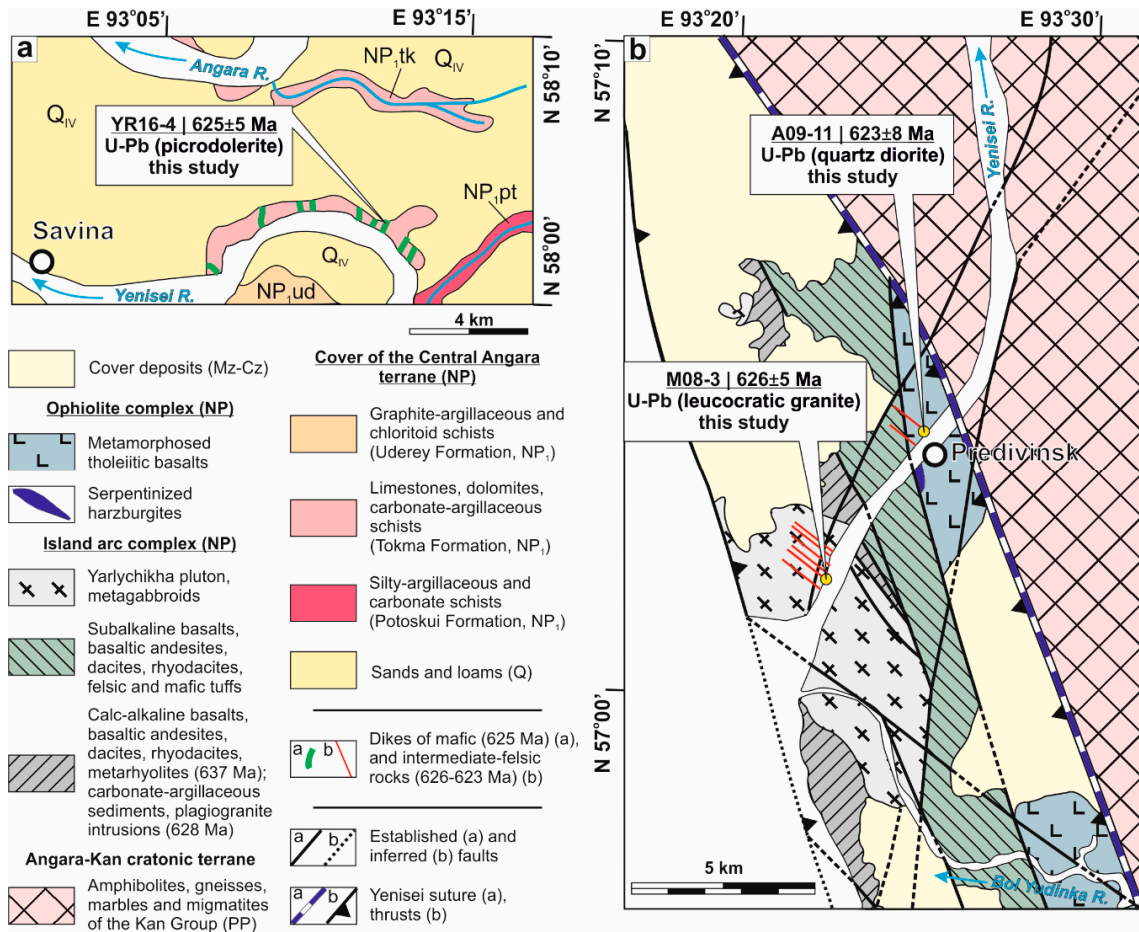


Figure 2. Position of the Ediacaran mafic rocks from dikes in the southwestern margin of the Central Angara terrane of the Yenisei Ridge, Savinsky Rock location, modified from state geological maps (a) and of the intermediate-felsic rocks from dikes in the imbricated structure of the Predivinsk island arc and ophiolite terrane, modified after [24] (b).

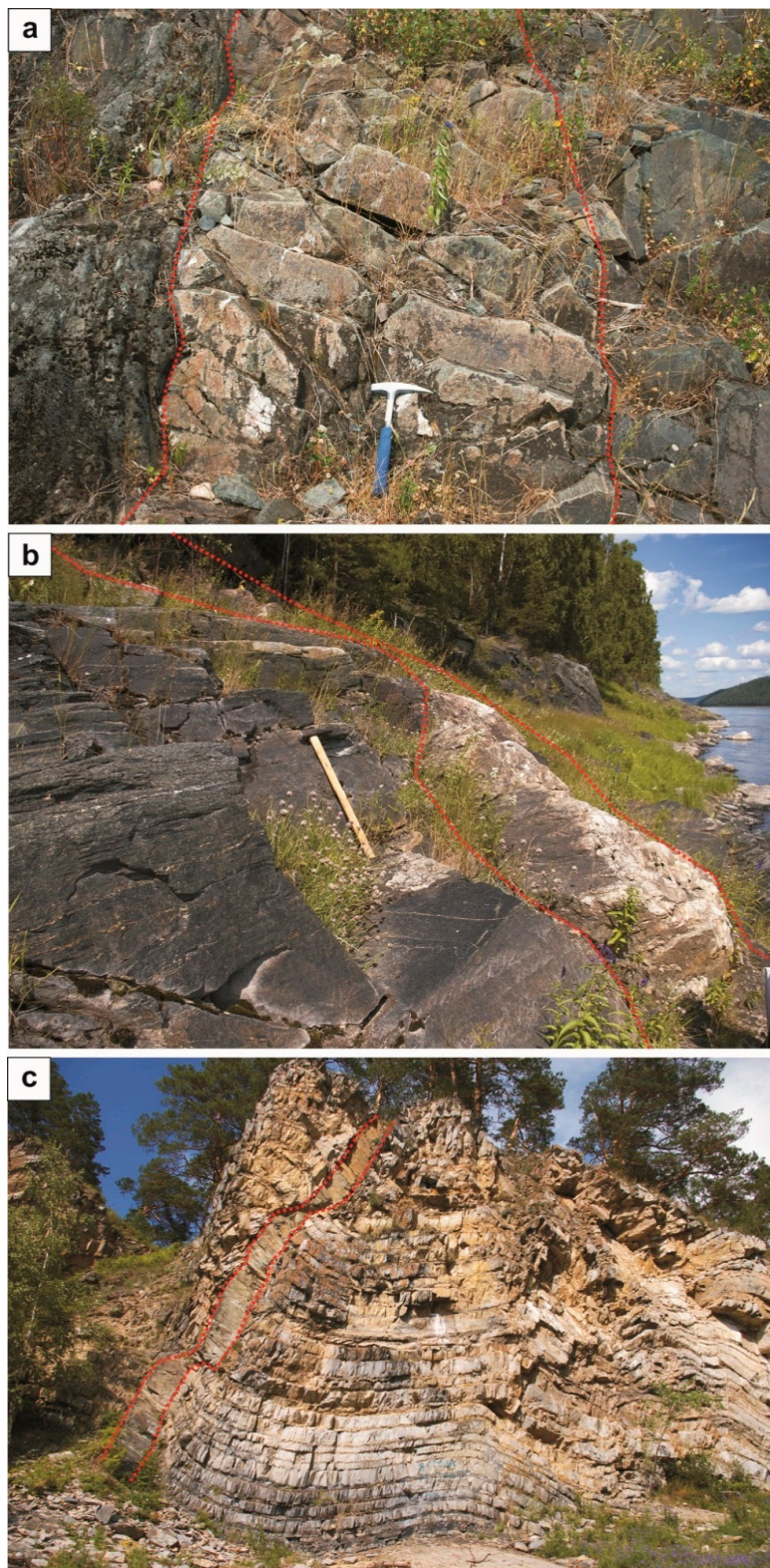


Figure 3. Photographs of some of the studied dikes: (a)—quartz diorite dike A09-11; (b)—leucocratic granite dike M08-3; (c)—one of the dolerite dikes.

3. Analytical Methods

The results of studies of the chemical composition of the minerals are presented in the Supplementary Materials (Tables S1–S5). These studies were done using a MIRA 3 LMU scanning

electron microscope (Tescan Orsay, Brno, Czech Republic) in the Center of Collective Use of Multielement and Isotope Studies of V.S. Sobolev Institute of Geology and Mineralogy SB RAS (Novosibirsk, Russia) (analysts N.S. Karmanov and M.V. Khlestov). The instrument is fitted with an INCA Energy 450 XMax 80 microanalysis system (Oxford Instruments Nanoanalysis Ltd., High Wycombe, UK). The accelerating voltage was 20 kV, and the cathode-ray current was 1.5 nA. The time compilation was 15–20 s, and the resulting spectra were processed automatically. Relative standard deviation during analysis of the main components (concentration >10–15% when recalculated for corresponding oxides) did not exceed 1.5%, and for components with concentrations 1–10 wt.%—no more than 2.0%. Studies of secondary components with concentrations below 1 wt.% were qualitative. FeO and Fe₂O₃ were obtained by stoichiometric calculation. The whole-rock Mg-number was calculated as $Mg\# = Mg^{2+}/(Mg^{2+} + Fe^{2+})$.

Results of whole rock X-ray fluorescence and ICP-MS analyses for the dikes are given in Table 1.

Whole rock X-ray fluorescence analyses were performed on a S4 Pioneer or a S8 Tiger spectrometer (Bruker AXS, Karlsruhe, Germany) with the 4-kW X-ray tube fitted with a Rh anode target disk according to the methodology in [27]. Samples for analysis were homogenized by fusing with a flux (mix of lithium metaborate and lithium tetraborate) in platinum crucibles in a TheOX electric fusion instrument (Claisse, Quebec City, QC, Canada) at 1050 °C. Melts were formed into radiator elements 32 mm in diameter. Weighted samples were 500 mg in mass, flux batches weighed 7.5 g. Calibration used standard samples of rocks: SDU-1 (dunite), ST-2 (trap), SGD-1 (essexite-gabbro), SA-1 (siltstone), GBPg-1 (garnet-biotite plagiogneiss), SNS-2 (nepheline syenite), SSn-1 (synnyrite), SSV-1 (svyatonosite), SG-1 (albitized granite), SG-2 (alaskite granite), SG-3 (alkaline agpaite granite), SI-2 (dolomitized limestone).

All ICP-MS analyses were performed on an Agilent 7500ce and an Element2 double-focusing sector field mass analyzer (ref. Table 1) in A.P. Vinogradov Institute of Geochemistry SB RAS (Irkutsk, Russia) in accordance with the technique described in [28]. Chemical preparation of the samples varied depending on their composition. Mafic rocks and some intermediate rocks were digested in open systems with a mix of acids (HF/HNO₃/HClO₄). Mafic rocks with low elements contents were digested in autoclaves (using a mix of HF/HNO₃ under high pressure with added HClO₄). Felsic rocks were fused with anhydrous lithium metaborate. Weighted samples were 100 mg in mass, all HNO₃ solutions had 2–3% acidity, final dilution factor of the samples solutions was 4000–5000 for open system and autoclave dissolution and 10,000 for fusion. Autoclave digestion was performed on a NPVF ANKON-AT analytical system. Fusion was performed using a VCHG-4 high-frequency induction furnace (“OOO Kristall” factory, Taganrog, Russia). HNO₃, HCl, and HF acids were either of ultrahigh purity according to GOST or of the Suprapure brand, their purification was done on a subPUR/duo PUR Milestone microwave laboratory system, and then a Savillex DST-1000 sub-boiling distillation system. Water was purified using a Millipore-ELIX-3 (Millipore SA, France) system. Element concentrations were determined using graduation by certified CLMS-1-4 solutions (SPEX, USA) with element concentrations 0.1, 1.0, and 5.0 ng/mL and signal drift control using ¹⁰³Rh as inner standard. Detection limits were estimated by standard method: $C_{\text{contr}} + 3\sigma$, where C_{contr} is the mean value of the control experiment, and σ is the relative mean square deviation of measurements (when recalculating for hard sample the dilution coefficient was taken into account). The relative error standard for repeatability (sr, %) was estimated from independent repeated analyses of samples (new dissolution, different analysts, measurements in different days). For state standard reference samples of different compositions, sr was in the range of 5–15% for elements with concentrations above the detection limit.

Correctness of analytical results was checked against approved standard rocks samples: JB-2 (basalt), JGb-1 (gabbro), JG-3 (granodiorite) from Japan; STM-1 (syenite) from the USA; SG-3 (alkaline agpaite granite), ST-2A (trap), SGD-2A (essexite-gabbro) from IG SB RAS, Russia.

Table 1. Chemical composition of the dike rocks.

Sample/Component	04ek07	A09-15-1	A09-16-1	YR-16-4	A09-17	A09-16-2	04ek10	A09-15	04ek06	04ek02	A09-11	M08-3	M08-2	Detection Limits			
	1	2	3	4	5	6	7	8	9	10	11	12	13	7, 9	2–6, 8	11–13	1, 10
	Picrodolerites							Dolerites			Qu-Diorite		Leucocratic Granites				
SiO ₂ , wt. %	42.87	43.75	44.82	44.90	44.86	44.98	45.19	47.87	48.65	49.09	58.68	74.10	74.89	0.1	0.1	0.1	0.1
TiO ₂	1.53	1.39	1.14	1.16	1.45	1.08	1.25	1.32	1.26	1.30	0.80	0.09	0.02	0.005	0.005	0.005	0.005
Al ₂ O ₃	13.58	13.50	13.69	14.13	13.75	13.49	14.99	15.52	16.04	15.56	16.36	14.90	14.93	0.1	0.1	0.1	0.1
Fe ₂ O ₃ *	9.63	10.78	11.80	11.72	11.26	11.97	9.97	10.95	8.86	8.93	7.51	1.10	0.66	0.005	0.005	0.005	0.005
MnO	0.16	0.11	0.16	0.16	0.12	0.15	0.17	0.17	0.14	0.15	0.11	0.04	0.02	0.005	0.005	0.005	0.005
MgO	10.35	10.60	11.61	11.05	11.44	12.74	11.79	6.34	7.58	7.52	2.51	0.34	0.16	0.05	0.05	0.05	0.05
CaO	8.84	6.84	7.57	7.92	6.84	7.06	6.28	8.46	7.37	7.38	5.48	1.54	1.54	0.01	0.01	0.01	0.01
Na ₂ O	1.75	1.47	1.54	1.41	1.76	1.29	1.72	2.82	2.28	2.40	5.98	3.19	4.49	0.1	0.1	0.1	0.1
K ₂ O	0.69	0.45	0.66	0.70	0.85	0.57	0.98	0.55	0.48	0.59	0.48	3.81	2.85	0.01	0.01	0.01	0.01
P ₂ O ₅	0.25	0.20	0.17	0.17	0.21	0.17	0.19	0.18	0.18	0.19	0.17	0.05	0.03	0.01	0.01	0.01	0.01
LOI	9.13	11.20	6.65	6.46	7.43	6.38	6.17	6.12	5.97	5.57	2.12	0.79	0.29				
Total	98.78	100.29	99.81	99.78	99.97	99.88	98.70	100.30	98.81	98.68	100.20	99.95	99.88				
Rb, ppm	24.20	24.30	22.60	24.90	46.60	23.60	23.00	30.60	24.00	26.10	7.10	89.00	100	0.13	0.12	3.11	0.5
Sr	365	180	193	210	279	175	408	326	245	334	251	166	107	1.09	0.48	18	3.0
Y	20.80	13.80	14.80	16.00	16.00	14.80	13.80	18.80	18.00	21.50	33.00	3.50	5.9	0.022	0.022	0.12	0.1
Zr	123.00	65.50	76.00	83.30	98.60	76.10	n.d.	100.00	107.00	89.30	n.d.	60.00	45	0.32	0.49	5.2	0.22
Nb	22.10	17.40	12.40	13.20	23.00	12.00	9.20	21.30	21.00	23.90	5.90	7.20	4.28	0.055	0.046	0.10	0.09
Ba	637	185	2808	3451	261	1241	248	265	279	384	595	604	218	3.09	4.37	12.3	5.5
La	25.20	14.30	15.50	15.30	17.60	13.60	16.00	17.90	14.70	17.30	10.80	2.89	2.27	0.081	0.11	0.92	0.06
Ce	50.20	27.00	31.20	29.70	35.10	27.10	34.00	34.00	34.00	34.10	26.00	7.40	4.43	0.074	0.096	0.99	0.06
Pr	6.80	3.41	3.40	3.61	4.17	3.00	3.73	4.11	3.72	4.80	3.73	1.04	0.6	0.012	0.011	0.036	0.03
Nd	26.50	15.10	13.90	14.90	16.80	13.30	17.00	16.20	17.00	18.40	18.00	4.54	2.56	0.039	0.37	0.14	0.03
Sm	5.36	3.32	2.98	3.13	3.48	2.89	3.33	3.62	3.64	4.18	4.89	1.35	0.9	0.0081	0.011	0.036	0.01
Eu	1.60	1.15	0.95	0.93	1.19	0.91	1.18	0.94	1.23	1.32	1.80	0.28	0.3	0.0027	0.0046	0.027	0.003
Gd	5.76	3.97	3.69	3.91	4.25	3.52	3.58	4.19	3.96	4.64	6.20	1.40	1.08	0.0095	0.021	0.037	0.02
Tb	0.80	0.54	0.53	0.56	0.59	0.49	0.46	0.62	0.58	0.77	1.06	0.21	0.17	0.0081	0.047	0.018	0.01
Dy	4.48	2.93	3.23	3.19	3.48	2.85	3.08	3.57	3.92	4.33	7.10	1.14	1.06	0.0065	0.0099	0.035	0.01
Ho	0.88	0.57	0.61	0.64	0.67	0.59	0.51	0.73	0.69	0.85	1.55	0.19	0.2	0.0017	0.0016	0.015	0.003
Er	2.24	1.45	1.80	1.84	1.91	1.68	1.41	2.05	1.88	2.48	4.67	0.55	0.5	0.0055	0.0089	0.22	0.02
Tm	0.32	0.20	0.24	0.25	0.24	0.23	0.19	0.28	0.28	0.39	0.73	0.07	0.1	0.0007	0.0019	0.014	0.01
Yb	1.92	1.18	1.59	1.60	1.60	1.46	1.14	1.77	1.64	2.17	5.20	0.44	0.67	0.0030	0.0098	0.027	0.02
Lu	0.32	0.17	0.24	0.25	0.23	0.24	0.16	0.26	0.25	0.31	0.79	0.06	0.1	0.0006	0.0015	0.017	0.003
Hf	3.76	1.54	1.96	2.70	2.61	1.86	n.d.	2.69	2.33	2.86	n.d.	2.45	1.54	0.017	0.034	n.d.	0.09
Ta	1.36	1.01	0.66	0.75	1.29	0.64	n.d.	1.16	1.20	1.32	0.49	0.49	0.57	0.043	0.068	0.0057	0.15
Th	4.56	1.98	1.84	1.88	2.66	1.71	2.11	1.91	2.46	2.24	9.90	4.87	3.23	0.025	0.027	0.11	0.03
U	1.04	0.59	0.38	0.40	0.60	0.35	0.38	0.46	0.53	0.62	0.78	1.17	0.36	0.0068	0.0051	0.053	0.02
Na ₂ O + K ₂ O	2.44	1.92	2.20	2.11	2.61	1.86	2.70	3.37	2.76	2.99	6.46	7.00	7.34				
Na ₂ O/K ₂ O	2.54	3.27	2.33	2.01	2.07	2.26	1.76	5.13	4.75	4.07	12.46	0.84	1.58				
Σ REE	132.38	75.29	79.86	79.81	91.31	71.86	85.77	91.84	87.49	96.04	92.52	21.56	14.94				
(La/Yb) _{CN}	8.92	8.23	6.62	4.95	7.47	6.33	9.53	6.87	6.09	5.42	1.41	4.46	2.30				
(La/Sm) _{CN}	2.94	2.69	3.25	3.05	3.16	2.94	3.00	3.09	2.52	2.58	1.38	1.34	1.58				
(Gd/Yb) _{CN}	2.43	2.72	1.88	1.51	2.15	1.95	2.54	1.92	1.95	1.73	0.96	2.57	1.30				
Eu/Eu*	0.88	0.97	0.87	0.81	0.94	0.87	1.04	0.74	0.99	0.91	1.00	0.62	0.93				
(Tb/Y) _{PM}	1.67	1.73	1.56	1.52	1.60	1.44	1.45	1.43	1.40	1.56	1.40	2.61	1.25				
Mg#	51.80	49.58	49.59	48.53	50.40	51.56	54.18	36.67	46.12	45.71	25.05	23.61	19.51				

Note. 1–7, picrodolerites; 8–10, dolerites; 11, quartz diorite; 12–13, leucocratic granites. Total iron given as Fe₂O₃*. LOI—loss on ignition; n.d.—no data. Element contents in ratios are normalized for chondrite [29] and primitive mantle [30]. Eu/Eu* = Eu_{CN}/[Gd_{CN} × Sm_{CN}]^{0.5}. Mg# = 100*MgO/(MgO + Fe₂O₃*) with oxides in molar proportions. Mg# calculated for all samples on anhydrous basis.

U-Th-Pb isotope analyses of zircons from the studied dike rocks (picrodolerite, quartz diorite and leucocratic granite) isolated by standard methodology using heavy liquids and magnetic separation were carried out on the SHRIMP-II SIMS of the Centre of Isotopic Research of VSEGEI (Saint Petersburg, Russia). The zircons were cast in Buehler EpoKwick resin along with standard Temora [31] and 91500 zircons [32]. Then the zircons were half-sectioned and finally polished. Transmitted and reflected light images as well as BSE and CL microphotographs were taken for guidance during analyses.

In-situ U-Pb analyses were performed, applying a secondary electron multiplier in peak-jumping mode following the procedure described in [33]. The analytical data were acquired for nine mass-stations ($^{196}\text{Zr}_2\text{O}$ to $^{254}\text{UO}_2$) with four to five mass-spectra per individual analysis. The Temora zircons were used as the primary Pb/U standard [31], while the 91500 zircon [32] was employed as U concentration and secondary standard, allowing Pb, U, and Th concentrations calculation. Each 5th analysis was done on the Temora zircon, making no less than 10 analyses per analytical session, and ran from a single mount or >20 if two mounts were analyzed during a single session. Uncertainties of the Temora measurements for the entire analytical session are given in the Table 2 footer. The 91500 zircon has been analyzed twice (at least) in the beginning and the end of the analytical session, revealing instrumental drift (if any occurred). The collected results were processed with the SQUID v1.13 [34] and ISOPLOT/Ex 3.22 [35] software. Common lead was corrected using measured $^{204}\text{Pb}/^{206}\text{Pb}$ and model values of Stacey and Kramers [36].

Table 2. Results of U-Th-Pb isotope investigations

Analyt. spot No.	Content, ppm				Isotope Ratios						Age, Ma		% D
	U	Th	²⁰⁶ Pb*	²³² Th/ ²³⁸ U	% ²⁰⁶ Pb _c	(1)	(1)	(1)	(1)	Err. corr.	(1)	(1)	
						²³⁸ U/ ²⁰⁶ Pb*	²⁰⁷ Pb*/ ²⁰⁶ Pb*	²⁰⁷ Pb*/ ²³⁵ U	²⁰⁶ Pb*/ ²³⁸ U		²⁰⁶ Pb/ ²³⁸ U	²⁰⁷ Pb/ ²⁰⁶ Pb	
(±%)													
Sample YR16-4 (GPS coordinates: N 58°01'09.18"; E 93°12'17.46")													
12.1	150	159	12.8	1.10	n.d.	10.0 ± 1.4	0.0629 ± 3.4	0.87 ± 3.7	0.100 ± 1.4	0.4	613 ± 8	705 ± 72	+14
16.1	32	26	2.72	0.85	0.00	10.0 ± 2.3	0.0622 ± 4.7	0.86 ± 5.2	0.100 ± 2.3	0.4	615 ± 14	682 ± 99	+10
23.1	83	58	7.19	0.72	0.56	9.9 ± 1.7	0.0604 ± 6.1	0.84 ± 6.3	0.101 ± 1.7	0.3	617 ± 10	619 ± 132	+0
4.1	49	38	4.29	0.79	0.22	9.91 ± 1.9	0.065 ± 6.3	0.905 ± 6.5	0.1009 ± 1.9	0.285	620 ± 11	776 ± 130	25
17.1	125	117	10.9	0.97	1.29	9.9 ± 1.5	0.0608 ± 6.5	0.85 ± 6.7	0.101 ± 1.5	0.2	621 ± 9	633 ± 140	+2
7.1	236	276	20.6	1.21	0.31	9.89 ± 1.2	0.0617 ± 3.3	0.86 ± 3.5	0.1011 ± 1.2	0.336	621 ± 7.1	663 ± 72	7
5.1	33	24	2.91	0.75	2.13	9.86 ± 2.7	0.06 ± 18	0.84 ± 18	0.1013 ± 2.7	0.146	622 ± 16	608 ± 390	-2
6.1	53	32	4.68	0.63	0.40	9.87 ± 2.2	0.0611 ± 5	0.854 ± 5.4	0.1013 ± 2.2	0.404	622 ± 13	644 ± 110	3
25.1	194	248	16.9	1.32	0.12	9.8 ± 1.3	0.0582 ± 2.5	0.81 ± 2.8	0.102 ± 1.3	0.5	624 ± 8	536 ± 55	-17
1.1	31	25	2.77	0.83	1.47	9.82 ± 2.4	0.0537 ± 16	0.75 ± 16	0.1017 ± 2.4	0.149	624 ± 14	359 ± 360	-43
18.1	260	320	22.7	1.27	0.18	9.8 ± 1.2	0.0626 ± 2.3	0.88 ± 2.6	0.102 ± 1.2	0.5	625 ± 7	694 ± 50	+10
11.1	147	150	12.9	1.05	n.d.	9.8 ± 3.4	0.0579 ± 2.7	0.81 ± 4.3	0.102 ± 3.4	0.8	626 ± 21	526 ± 58	-20
2.1	52	39	4.67	0.78	1.50	9.78 ± 2	0.0617 ± 12	0.87 ± 12	0.1021 ± 2	0.164	627 ± 12	664 ± 260	6
10.1	80	65	7.07	0.83	0.36	9.79 ± 1.7	0.0604 ± 7.1	0.851 ± 7.3	0.1021 ± 1.7	0.232	627 ± 10	618 ± 150	-1
13.1	67	50	5.89	0.77	0.31	9.8 ± 1.8	0.0660 ± 4.9	0.93 ± 5.2	0.102 ± 1.8	0.3	627 ± 11	805 ± 103	+23
24.1	135	135	11.8	1.03	0.40	9.8 ± 1.5	0.0567 ± 4.8	0.80 ± 5.0	0.102 ± 1.5	0.3	627 ± 9	482 ± 106	-32
3.1	111	75	9.75	0.70	n.d.	9.74 ± 1.4	0.0631 ± 2.7	0.893 ± 3	0.1027 ± 1.4	0.472	630 ± 8.6	711 ± 57	13
22.1	101	56	8.9	0.58	0.43	9.7 ± 3.5	0.0589 ± 5.3	0.83 ± 6.3	0.103 ± 3.5	0.6	630 ± 21	564 ± 115	-12
14.1	76	52	6.72	0.70	1.49	9.7 ± 3.4	0.0580 ± 9.9	0.82 ± 10.5	0.103 ± 3.4	0.3	630 ± 20	531 ± 218	-20
20.1	85	78	7.59	0.94	n.d.	9.7 ± 1.7	0.0606 ± 6.5	0.86 ± 6.7	0.103 ± 1.7	0.2	634 ± 10	626 ± 140	-1
9.1	130	131	11.7	1.04	0.37	9.63 ± 1.5	0.0635 ± 3.7	0.909 ± 4	0.1038 ± 1.5	0.373	637 ± 9	726 ± 79	14
19.1	307	387	27.7	1.30	n.d.	9.5 ± 1.2	0.0592 ± 2.2	0.86 ± 2.5	0.105 ± 1.2	0.5	644 ± 7	575 ± 49	-13
15.1	35	36	3.17	1.07	0.64	9.5 ± 2.3	0.0620 ± 9.4	0.90 ± 9.7	0.105 ± 2.3	0.2	646 ± 14	675 ± 202	+5
Sample A09-11 (GPS coordinates N 57°04'36.90"; E 93°26'9.80")													
8.1	18	16	1.5	0.96	n.d.	10.12 ± 2.4	0.0585 ± 13.9	0.797 ± 14.1	0.0988 ± 2.4	0.2	608 ± 14	549 ± 303	-11
1.2	183	267	15.8	1.51	n.d.	10.00 ± 1.6	0.0603 ± 2.0	0.831 ± 2.5	0.1000 ± 1.6	0.6	614 ± 9	614 ± 43	-0
5.1	174	228	15	1.35	0.36	9.99 ± 1.4	0.0614 ± 2.8	0.848 ± 3.1	0.1001 ± 1.4	0.4	615 ± 8	654 ± 59	+6
4.1	55	50	4.73	0.94	0.20	9.97 ± 1.6	0.0637 ± 3.7	0.882 ± 4.1	0.1003 ± 1.6	0.4	616 ± 10	733 ± 79	+17
7.1	83	131	7.19	1.62	0.16	9.94 ± 1.5	0.0609 ± 3.3	0.845 ± 3.7	0.1006 ± 1.5	0.4	618 ± 9	637 ± 72	+3
2.1	122	117	10.5	0.99	0.35	9.91 ± 1.4	0.0611 ± 3.5	0.851 ± 3.8	0.1010 ± 1.4	0.4	620 ± 8	643 ± 75	+4
1.1	29	17	2.54	0.62	n.d.	9.82 ± 2.2	0.0600 ± 15.1	0.842 ± 15.2	0.1018 ± 2.2	0.1	625 ± 13	602 ± 326	-4
6.1	74	80	6.48	1.12	n.d.	9.80 ± 1.6	0.0607 ± 4.4	0.854 ± 4.7	0.1020 ± 1.6	0.3	626 ± 10	630 ± 95	+1
9.1	17	17	1.48	1.05	0.77	9.77 ± 2.5	0.0661 ± 11.0	0.933 ± 11.3	0.1024 ± 2.5	0.2	628 ± 15	810 ± 231	+24
3.1	95	84	8.37	0.91	n.d.	9.77 ± 1.5	0.0632 ± 3.7	0.893 ± 4.0	0.1024 ± 1.5	0.4	628 ± 9	716 ± 79	+13

Table 2. Cont.

Analyt. spot No.	Content, ppm					Isotope Ratios					Age, Ma		% D
	U	Th	²⁰⁶ Pb*	²³² Th/ ²³⁸ U	% ²⁰⁶ Pb _c	(1)	(1)	(1)	(1)	Err. corr.	(1)	(1)	
						²³⁸ U/ ²⁰⁶ Pb*	²⁰⁷ Pb*/ ²⁰⁶ Pb*	²⁰⁷ Pb*/ ²³⁵ U	²⁰⁶ Pb*/ ²³⁸ U		²⁰⁶ Pb/ ²³⁸ U	²⁰⁷ Pb/ ²⁰⁶ Pb	
Sample M08-3 (GPS coordinates: N 57°01'13.70"; E 93°22'12.30")													
6.1	6750	730	586	0.11	0.01	9.89 ± 1.3	0.0605 ± 1.1	0.843 ± 1.6	0.1011 ± 1.3	0.8	621 ± 7	622 ± 23	+0
10.1	7610	590	663	0.08	n.d.	9.86 ± 1.5	0.0603 ± 0.3	0.843 ± 1.5	0.1014 ± 1.5	1.0	623 ± 9	613 ± 8	-2
8.1	2210	44	193	0.02	0.01	9.84 ± 1.2	0.0605 ± 1.3	0.848 ± 1.8	0.1016 ± 1.2	0.7	624 ± 7	622 ± 29	-0
11.1	3207	64	280	0.02	0.04	9.84 ± 1.3	0.0614 ± 0.7	0.860 ± 1.4	0.1017 ± 1.3	0.9	624 ± 8	653 ± 15	+5
7.1	956	24	83.5	0.03	0.40	9.84 ± 1.4	0.0612 ± 2.1	0.858 ± 2.5	0.1017 ± 1.4	0.6	624 ± 8	646 ± 45	+4
1.1	3156	169	276	0.06	17.38	9.82 ± 3.3	0.0621 ± 10.2	0.871 ± 10.7	0.1018 ± 3.3	0.3	625 ± 20	677 ± 218	+8
4.1	2306	56	202	0.02	0.01	9.81 ± 1.2	0.0600 ± 0.5	0.844 ± 1.3	0.1019 ± 1.2	0.9	626 ± 7	605 ± 12	-4
2.1	2715	42	238	0.02	0.08	9.81 ± 1.2	0.0599 ± 0.5	0.842 ± 1.3	0.1020 ± 1.2	0.9	626 ± 7	600 ± 11	-5
9.1	1400	17	123	0.01	0.08	9.77 ± 1.2	0.0617 ± 0.7	0.870 ± 1.4	0.1024 ± 1.2	0.9	628 ± 7	662 ± 15	+5
12.1	630	6	55.5	0.01	0.06	9.76 ± 2.5	0.0605 ± 3.3	0.855 ± 4.1	0.1025 ± 2.5	0.6	629 ± 15	623 ± 71	-1
5.1	2676	40	236	0.02	n.d.	9.74 ± 1.2	0.0612 ± 0.5	0.866 ± 1.3	0.1026 ± 1.2	0.9	630 ± 7	645 ± 11	+3
2.2	74	48	7.74	0.67	0.36	8.24 ± 1.7	0.0650 ± 3.4	1.088 ± 3.8	0.1213 ± 1.7	0.4	738 ± 12	775 ± 71	+5
3.1	319	127	34	0.41	1.53	8.08 ± 1.3	0.0659 ± 3.3	1.125 ± 3.5	0.1238 ± 1.3	0.4	752 ± 9	805 ± 69	+7
1.2	81	69	9.5	0.88	n.d.	7.32 ± 1.6	0.0663 ± 4.0	1.249 ± 4.3	0.1366 ± 1.6	0.4	825 ± 12	817 ± 84	-1

Note. Uncertainties are given at the 1σ level; ²⁰⁶Pb_c and ²⁰⁶Pb* are common and radiogenic lead respectively; (1)—common lead corrected from measured ²⁰⁴Pb. For samples A09-11 and M08-3 the TEMORA1 standard calibration error is 0.46%; for sample YR16-4—0.30% (Series 1) and 0.52% (Series 2). D—discordance. n.d.—no data.

4. Results

4.1. Petrography and Mineralogy

Picrodolerites have a medium-grained structure and an ophitic texture and porphyry phenocrysts of plagioclase, clinopyroxene, and olivine 0.5–1 mm in size. Plagioclase has a labradorite composition (X An from 0.51 to 0.69) and contains low contents of K₂O, MgO, and FeO as well as BaO in individual samples (Supplementary Materials Table S1, Figures 4a and 5a). In rims, the labradorite is replaced by andesine and albite. Clinopyroxene corresponds to augite with a composition approaching diopside (Table S2, Figure 4a). This mineral has Mg# up to 0.78 and insignificant contents of TiO₂, Na₂O, and Cr₂O₃. Phlogopite-annite (grains up to 0.03 mm in size) is pleochromatic in light-brown and brownish-red colors, located in interstices between grains of rock-forming minerals and replaced by chlorite (Table S3, Figure 4b). In it we detected high contents of MgO up to 13.95 wt.%, Mg# up to 0.56, and low concentrations of Al₂O₃ (11.28–13.15 wt.%) as well as TiO₂, CaO, MnO, Na₂O, and Cl. Olivine is replaced by talc with high MgO content (up to 28.32 wt.%) and has rims of chrome-magnetite up to 40 micron wide (FeO = 46.6–67.4 wt.%; Fe₂O₃ = 29.8–31.6 wt.%; Cr₂O₃ up to 10.3 wt.%; and insignificant contents of Al₂O₃ and MgO). The composition of olivine probably corresponded to forsterite due to high Mg# of clinopyroxenes of this rock. Inclusions in rock-forming minerals include chromespinelides: Magnesiochrompicotite, subferrialumochromite and alumochromite (Al₂O₃ = 18.4–37.8 wt.%; Fe₂O₃ = 6.54–16.6 wt.%; Cr₂O₃ = 22.9–28.3 wt.%; FeO = 6.70–39.1 wt.%; MgO up to 14.7 wt.%), which have chrome-magnetite reaction rims around the grains. The groundmass contains titanomagnetite with ilmenite inclusions. Auxiliary minerals are apatite, zircon, and monazite (Figure 4c). Barite associating with calcite, dolomite, and sulfides (pyrite, chalcopyrite, pyrrhotite, pentlandite, and smythite) occurs in the form of thin veinlets (up to 0.01 mm) in chlorite (Figure 4b).

Dolerites are fine- and medium-grained with ophitic texture mainly consisting of plagioclase and pyroxene and a small amount of dark mica. The plagioclase (grains up to 0.3 mm) corresponds to labradorite (X An = 0.65–0.50) with trace contents of FeO, MgO, and K₂O (Table S1, Figures 4a and 5a). Labradorite has reaction rims of albite. Clinopyroxene (grains up to 0.5 mm) is represented by augite close in composition to the augite in picrodolerites (Table S2, Figures 4d and 5b). The composition of dark mica corresponds to phlogopite-annite (Al₂O₃ up to 13.87 wt.%; Mg# up to 0.50) with lower concentration of TiO₂ (3.45 wt.%) compared to the same mineral from picrodolerites. This mica contains CaO, MnO, and Cl (Table S3, Figure 4d). Dolerites include shots of sulfide minerals—Pyrite and chalcopyrite. Pyrite contains galena and sphalerite inclusions (Figure 4e).

Quartz diorites are medium-grained, mostly consisting of plagioclase, up to 30 vol.% of amphibole phenocrysts (up to 7 mm), some quartz (no more than 15 vol.%), and individual pyroxene grains. Quartz is represented by small recrystallized grains (<0.5 mm). The composition of plagioclase corresponds to oligoclase (X An = 0.10–0.22 a.p.f.u.) (Table S1, Figures 4f and 5a). Amphibole has the composition of magnesian hornblende: SiO₂ up to 44.46 wt.%; MgO up to 11.31 wt.%; CaO up to 11.92 wt.%; Na₂O up to 1.58 wt.%, and Mg# up to 60 (Table S4, Figure 4f). Pyroxene from fragments of relict grains (up to 0.4 mm) corresponds to augite and contains trace concentrations of NaO, TiO₂, and MnO (Table S2, Figures 4f and 5b). Hornblende is replaced by pargasite (SiO₂ up to 42.46 wt.%; MgO up to 9.55 wt.%; CaO up to 11.97 wt.%; Na₂O up to 1.91 wt.%, K₂O up to 1.28 wt.%; Al^{VI} up to 0.61 a.p.f.u.; Fe³⁺ up to 0.34 a.p.f.u.; Mg# up to 0.52) (Table S4, Figure 4f). Pargasite is replaced with biotite that is close in composition to the phlogopite-annite series (Al₂O₃ up to 15.27 wt.%; Mg# up to 0.58) and has insignificant MnO content (Table S3, Figure 4f). Amphiboles have trace concentrations of Cl. Auxiliary and opaque minerals are zircon, apatite, titanite, titanomagnetite, magnetite, and ilmenite.

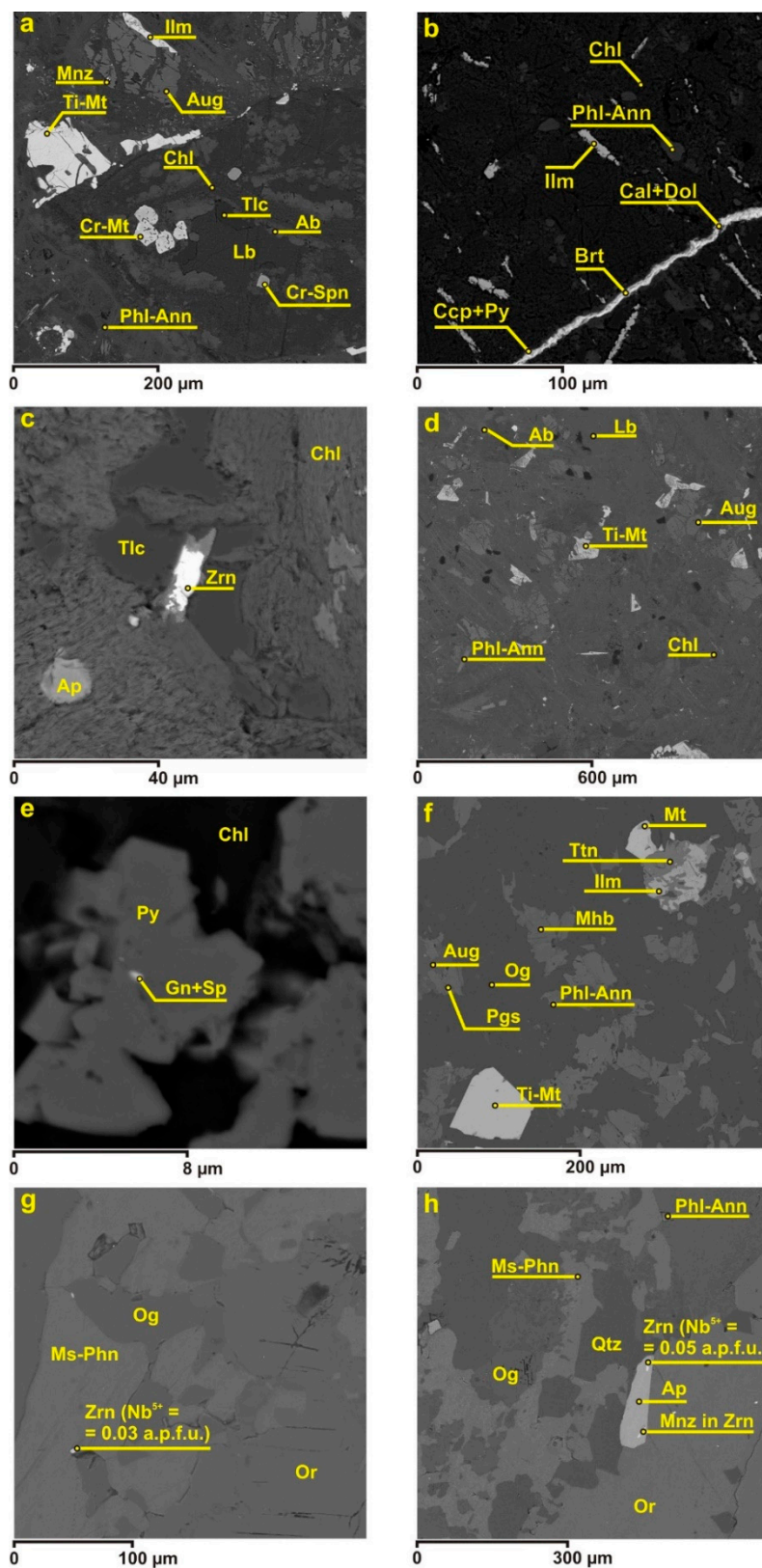


Figure 4. Back-scattered electron images of minerals from the dike rocks: (a–c)—picrodolerites (sample YR16-4), (d)—dolerite (sample A09-15), (e)—dolerite (sample A09-15-1), (f)—quartz diorite (sample A09-11), (g,h)—leucocratic granites (sample M08-03). Mineral names abbreviations—from [37].

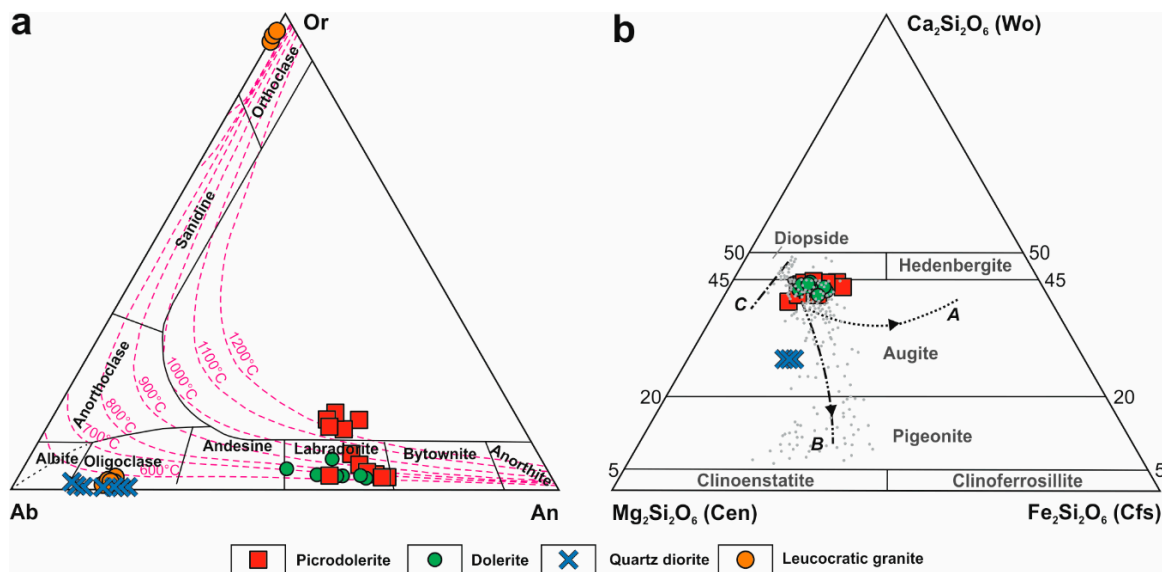


Figure 5. Composition of minerals from the dike rocks on classification diagrams: for plagioclases from [38] (a), for clinopyroxenes from [39] (b). Composition lines for clinopyroxenes are given for igneous rocks of: *A*—intraplate settings, picrites, subalkaline gabbros and syenites, Skaergaard intrusion, Greenland [40]; *B*—active continental margin settings, basalts, basaltic andesites, dacites, Hudson Volcano, Chilean Patagonia [41]; *C*—island arcs, basalts and gabbros, back-arc basins Ispendere, Malatya, southwestern Anatolia [42]. Arrows on lines *A* and *B* show directions of changes in pyroxenes compositions with rising SiO_2 content in the rocks. Grey dots show compositions of clinopyroxenes from basalts associating with high-K rocks of the Kuril Islands and the Kamchatka active continental margin from [43].

Leucocratic granites are medium-grained and consist mostly of plagioclase, potassium feldspar, and quartz. Plagioclase corresponds to oligoclase in composition ($X_{\text{An}} = 0.16\text{--}0.18$) and has low contents of K_2O ; K-feldspar ($X_{\text{Or}} = 0.94\text{--}0.96$) with low Na_2O content (Table S1, Figure 4g,h and Figure 5a). Biotite (grains up to 0.08 mm) corresponding to phlogopite-annite ($\text{Al}_2\text{O}_3 = 15.34$ wt.%; Mg\# up to 0.53) and occurs as inclusions in plagioclase. Like in quartz diorites, this mineral contains trace concentrations of MnO (Table S3, Figure 4h). Auxiliary minerals include large (up to 1.5 mm), weakly deformed subparallel grains of light mica underlining the weak gneissic banding in the rock. This mica corresponds to phengite muscovite ($\text{FeO} + \text{Fe}_2\text{O}_3 = 3.32\text{--}5.03$ wt.%; MgO up to 1.72 wt.%) with insignificant contents of TiO_2 and Na_2O (Table S5, Figure 4g,h). The rock also contains epidote, zircon, apatite, rutile, and ilmenite.

4.2. Geochemistry

The geochemical particularities of the mafic, intermediate, and felsic rocks reflected both their similarities and differences (Table 1).

The mafic rocks form two groups on the TAS diagram from Le Maitre et al. [44] (Figure 6) and plot in the fields of picrobasalts (picrodolerites) and basalts (dolerites). The former have low concentrations of SiO_2 (42.87–45.19 wt.%) and $\text{Na}_2\text{O} + \text{K}_2\text{O}$ (1.86–2.7 wt.%), and elevated concentrations of MgO (10.35–12.74 wt.%) and Mg\# (48.53–54.18); the latter have more elevated concentrations of SiO_2 (47.87–49.09 wt.%) and $\text{Na}_2\text{O} + \text{K}_2\text{O}$ (2.76–3.37 wt.%), and decreased concentrations of MgO (6.34–7.58 wt.%) and Mg\# (36.67–46.12) (Table 1). In addition, some of the samples from the first group with the highest MgO content (~12 wt.% and higher) correspond to picritic rocks according to the classification of Le Bas [45]. The mafic rocks have high $\text{Na}_2\text{O}/\text{K}_2\text{O}$ ratios (2.0–5.1), and of the $\text{FeO}^*/\text{MgO}\text{--}\text{SiO}_2$ diagram [46], they plot in the field of the tholeiitic series (Figure 7). These rocks have significant similarities in distributions of REE and on spider diagrams (Figure 8). They have either

small or no Eu anomalies, low $(La/Sm)_N$ and $(Gd/Yb)_N$ ratios (1.51–2.43) and (2.52–3.25), moderate $(La/Yb)_N$ ratios (4.95–9.53) and Σ REE values (71.86–132.38 ppm) (Table 1, Figure 8a). The rocks of the first group in most samples are distinguished by their higher $(La/Yb)_N$ values and closer similarity of trace element distributions to that of OIB. These dike rocks are enriched in large-ion elements—Ba (up to 3451 ppm) and Rb (up to 46.6 ppm) with concentrations that are close to such rocks in OIB, as well as Sr (up to 408 ppm) with concentrations close to transitional rocks between OIB and E-MORB (Table 1, Figure 8b). The mafic rocks have high concentrations of high field strength elements: REE, Th, U, Nb, Ta, Hf, and Zr—Close to those of rocks between OIB and E-MORB.

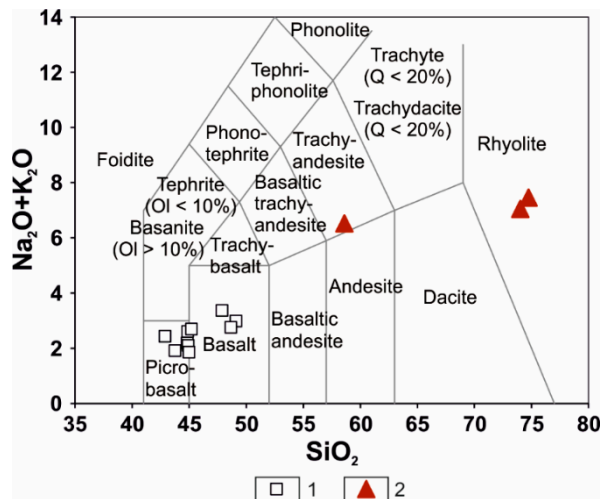


Figure 6. TAS diagram of [44] for the mafic (1) and intermediate-felsic (2) rocks.

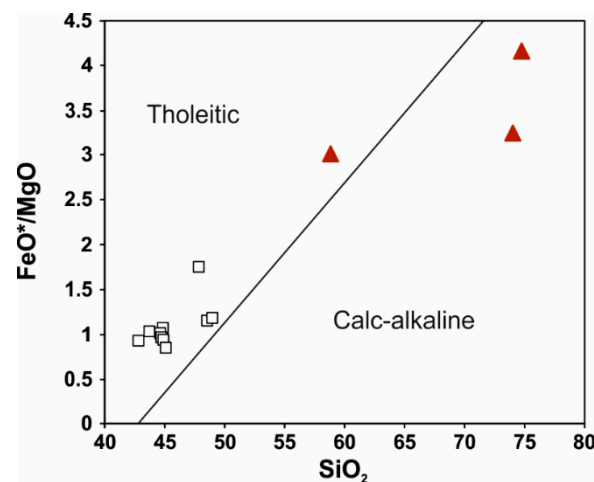


Figure 7. FeO^*/MgO vs SiO_2 diagram from [46] for the mafic and intermediate-felsic rocks. Symbols -ref. Figure 6. FeO^* is total iron.

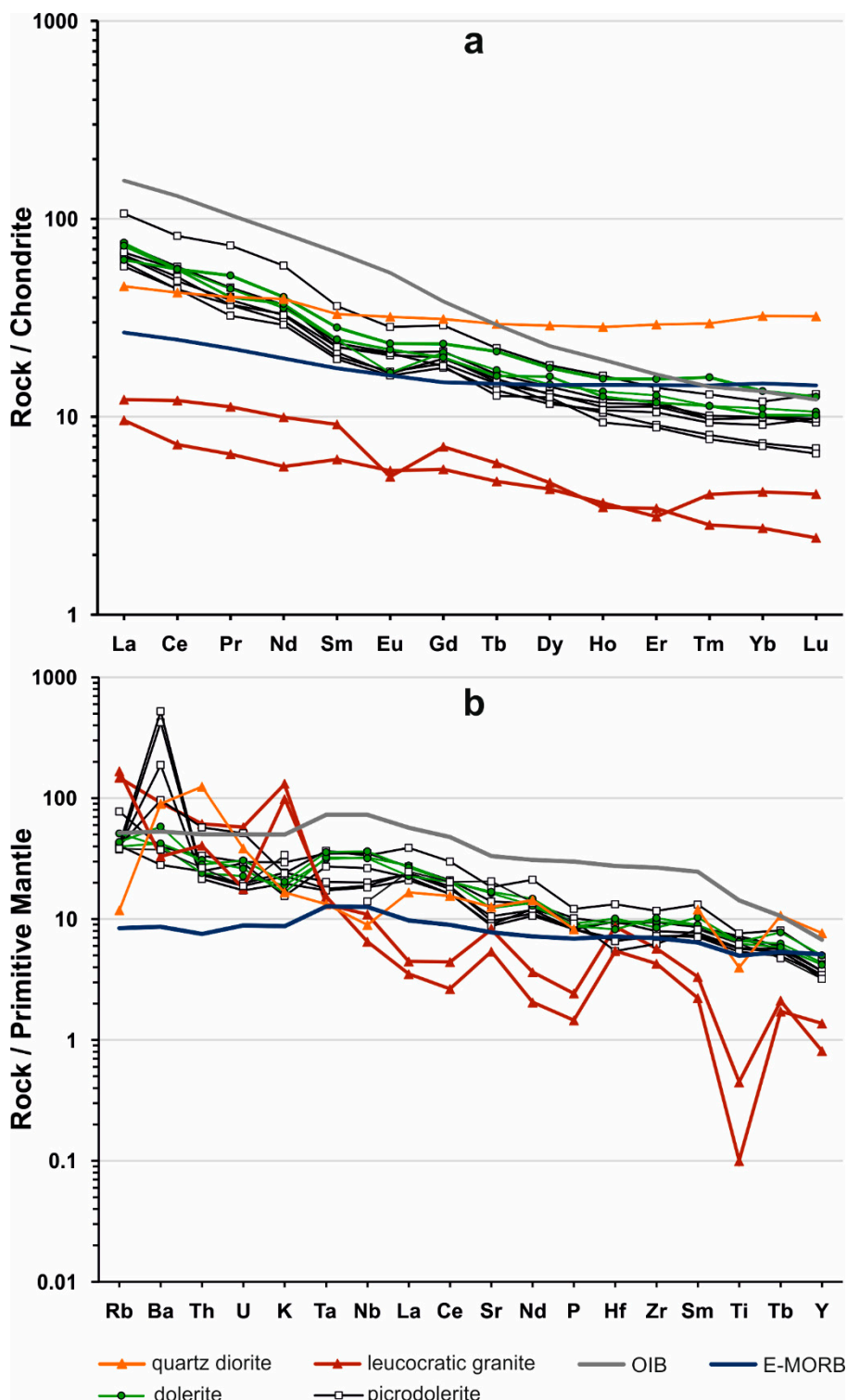


Figure 8. REE (a) and spider (b) diagrams for the mafic-intermediate-felsic rocks. Elements contents are normalized for chondrite [29] and primitive mantle [30].

Other studied dikes on the TAS diagram (Figure 6) correspond to intermediate rocks (quartz diorite) with moderate contents of SiO₂ (58.68 wt.%) and Na₂O+K₂O (6.46 wt.%), and high Na₂O/K₂O ratio (12.46), and felsic rocks (leucocratic granite) with high contents of SiO₂ (74.1–74.89 wt.%), and plot respectively in the fields of tholeiitic and calc-alkaline series (Figure 7).

The felsic rocks show the most differentiated trace elements distributions. They have high positive anomalies for large-ion elements (K, Rb, and in some samples—Ba) with concentrations higher than equivalents for OIB, as well as Sr with concentrations close to E-MORB. They also have low negative anomalies for most high field strength elements (especially Ti). Concentrations of Th, U, Ta, and Hf are close to rocks between OIB and E-MORB. The felsic rocks either do not have or have moderate Eu anomalies and are distinguished by low values of Σ REE (up to 21.56 ppm) and moderate $(La/Yb)_N$ ratios (2.3–4.46). These rocks show a similar inclination of the REE distributions ($(La/Yb)_N = 2.3\text{--}4.46$) with rocks between OIB and E-MORB (Figure 8a).

The intermediate rocks have high concentrations of Ba, HREE, Hf, and Zr (higher than in OIB) and, together with mafic rocks, are characterized by $(Tb/Y)_N$ ratios between 1.4 and 1.73, which is close to OIB values. Concentrations of Th in these rocks are similar to those of island arc basalts. The intermediate rocks have flat REE distributions, no Eu anomalies, and LREE concentrations close to rocks between OIB and E-MORB.

4.3. Zircon Geochronology

The results of zircon geochronological studies are given in Figure 9 and Table 2. The ages discussed in the text and error ellipses in diagrams with the concordia are 2σ . Ratios and corresponding ages in Table 2 are given with 1σ errors.

Zircons from picrodolerite sample YR16-4 are mostly dipyrmidal-short prismatic, euhedral and subeuhedral, clear or slightly colored grains (Figure 9b). Individual grains can have a rounded form. There are few mineral or melt inclusions. Sometimes a concentric growth zoning can be observed in optical photos in transmitted light. CL images show that their structure consists in a combination of rounded (possibly due to reabsorption) dark central cores and bordered by lighter rims with concentric or sector growth zoning. U/Pb SIMS analysis of 25 grains yielded a $^{206}\text{Pb}/^{238}\text{U}$ variation in the range 613–646 Ma (Table 2). Excluding two of the lowest values (probably due to Pb loss) and the highest three (possible contamination, considering the rounded shape of grains), the concordant age is 625 ± 5 Ma ($N = 20$, MSWD = 0.01, probability = 0.92) (Figure 9a). This date is most probably the crystallization age of the studied picrodolerite.

Zircons from quartz diorite sample A09-11 are mostly subeuhedral and euhedral dipyrmidal-prismatic grains, sometimes with ditetragonal dipyramid faces (Figure 9d). They have a noticeable amount of melt and mineral inclusions. Their inner structure, as observed in CL images, has a dark central core, in which concentric growth zoning often cannot be detected at the selected imaging parameters. Contours of the central parts are typically rounded, apparently due to partial reabsorption. The cores are bordered by light CL rims with concentric oscillatory and sector growth zoning. The structure and morphology of the zircons indicate their magmatic origin. Obtained $^{206}\text{Pb}/^{238}\text{U}$ analysis results are scattered, possibly due to Pb losses. Excluding the three lowest values, the concordant age is 623 ± 8 Ma ($N = 7$, MSWD = 2, probability = 0.16) (Table 2, Figure 9c), which corresponds to the time of crystallization for the quartz diorite.

Zircons in leucocratic granite sample M08-3 are mainly subeuhedral and euhedral, dipyrmidal-prismatic grains, weakly colored, clear or translucent. The tips of pyramids show growth structures (Figure 9f). CL images show varying cores, usually rounded with different zonation types, and surrounded by dark rims. Growth zoning is unclear on CL images but is discernible on some optical microphotos. Three zircons yield significantly older (825 ± 12 Ma, 752 ± 9 Ma and 738 ± 12 Ma) ages in their cores (1.2, 2.2, 3.1) and have low U, Th, and $^{206}\text{Pb}^*$ contents that are anomalous for this sample—These results were not counted in calculations. Excluding two results with the highest U contents and decreased $^{206}\text{Pb}/^{238}\text{U}$ ratios indicating Pb loss from metamict domains, the concordant age for 9 results is 626 ± 5 Ma ($N = 9$, MSWD = 0.045, probability = 0.83) (Table 2, Figure 9e). This age determines the time of magmatic crystallization of the leucocratic granite.

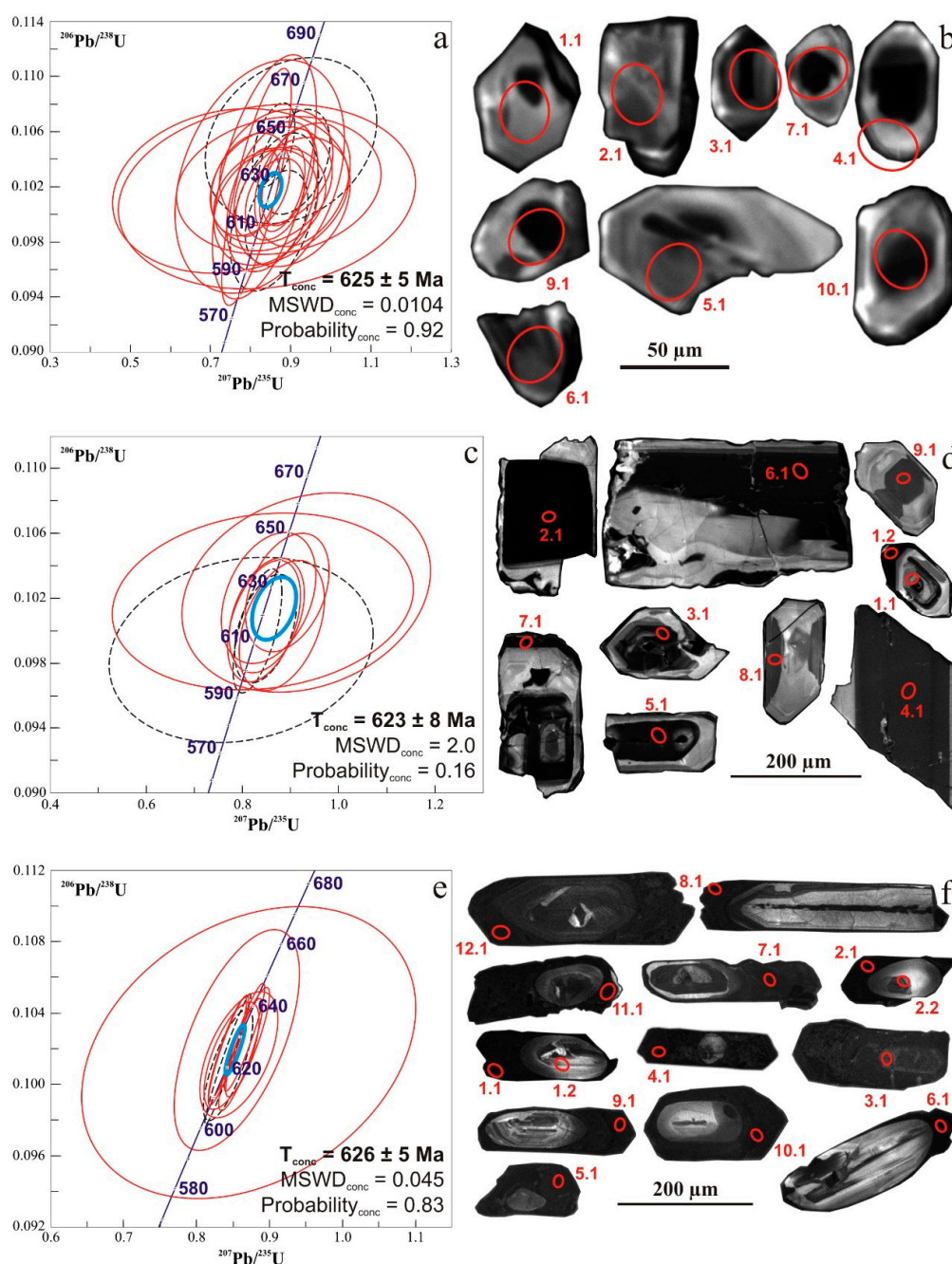


Figure 9. Concordia diagrams and CL images for zircons from picrodolerite sample YR16-4 (a,b), quartz diorite sample A09-11 (c,d) and leucocratic granite sample M08-3 (e,f). Red circles in the zircon CL images indicate the U/Pb isotopic analysis spots. The blue ellipse is the weighted-mean error ellipse.

5. Discussion

Results of geologic, mineralogical-petrographic, geochemical, and U-Pb geochronological investigations allowed us to identify an association of dikes of Ediacaran age (626–623 Ma). This complements available data on the Ediacaran magmatic history of the Yenisei Ridge and the entire western margin of the Siberian Craton. The rocks of this association, localized in the junction zone of the Tatarka-Ishimba and Yenisei sutures in the South Yenisei Ridge, are diverse in petrography—From picrodolerites-dolerites to quartz diorites and leucocratic granites, which in itself indicates that at this time, magmatism was affected by both mantle and crustal sources. Detailed mineralogical

studies showed that these rocks contain Mg-enriched rock-forming minerals and Th-, P-, Cr-, Ti-, and Zr-containing auxiliary minerals. These particularities, as well as the concentrations of large-ion and high field strength elements (Ba, Rb, Sr, Th, U, REE, Nb, Ta, Hf, and Zr) in the studied mafic tholeiitic rocks confirm the input of OIB and E-MORB mantle components in their magmatic source, as shown in (Figure 8). During their evolution, the mantle-sourced mafic melts assimilated some crustal material and formed Th-enriched dikes of intermediate composition and K- and Rb-enriched felsic rocks. Like the mafic rocks, the tholeiitic intermediate rocks retain close concentrations of large-ion and high field strength elements, such as Sr, Ce, Pr, Nd, Sm, and P. Whereas the felsic varieties have a slight similarity of concentrations with mafic rocks that can be observed for individual samples in Sr and Hf content, but also with the intermediate rocks in their Nb and Ta concentrations. The crustal material was probably of metasedimentary nature and pre-Cryogenian in age, which is indicated by U-Pb isotope studies of zircon cores from felsic rocks. On tectonic discrimination diagrams for Th/Yb vs. Nb/Yb from [47] (Figure 10a) and Th/Yb vs. Ta/Yb from [48] (Figure 10b), the mafic rocks appear in transition fields between E-MORB and OIB and between oceanic tholeiitic (TH) and alkalic (ALK) fields respectively. On the first diagram some of the samples plot in the field of volcanic arcs rocks, close to MORB—OIB. This agrees with the possibility of suprasubduction formation conditions for these rocks. Taking into account the composition data for pyroxenes from the dikes studied in the present paper, they could have formed in conditions of an active continental margin. The studied dikes are mostly non-deformed but intrude significantly deformed and weakly metamorphosed sedimentary rocks (metasandstones and marmorized limestones) and igneous rocks (gabbroids). The deformations in the latter are explained by previous tectonic events—the collision of the Central Angara terrane with the Siberian Craton and subsequent accretion of island arc blocks to it [10]. Weak deformations observed in the dikes themselves and in host metasedimentary rocks are related to subsequent tectonothermal events that manifested during the entire Ediacaran in conditions of the evolving transform margin. At the final stage, these tectonothermal processes took place synchronously with the emplacement of adakite dikes and associating gabbro-anorthosites 576–546 Ma that were formed in conditions of a transform active continental margin [14].

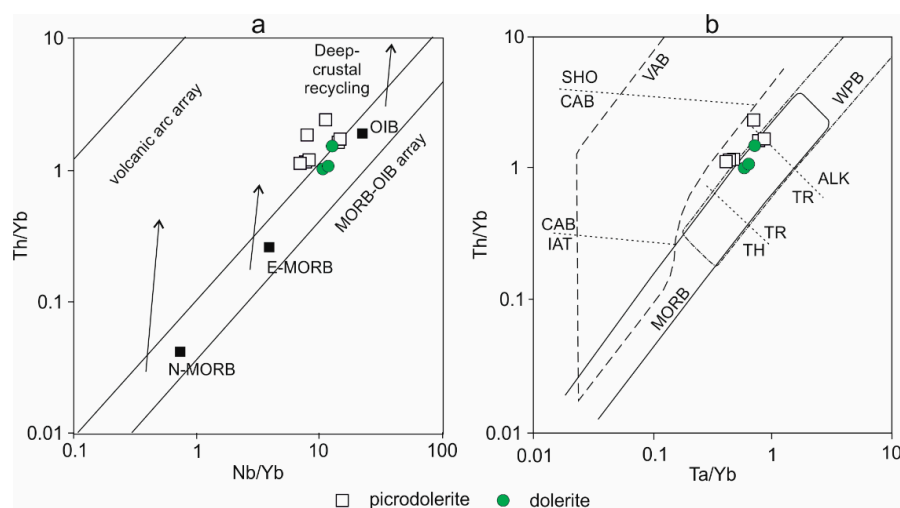


Figure 10. Tectonic discrimination diagrams for the mafic studied rocks. (a) Th/Yb vs. Nb/Yb from [47]; (b) Th/Yb vs. Ta/Yb from [48]. Abbreviations are the types of mafic volcanic rocks: MORB—middle ocean ridge basalts; N-MORB—normal of middle ocean ridge basalts; E-MORB—enriched of middle ocean ridge basalts; OIB—ocean islands basalts; WPB—within plates basalts; ALK—alkalic; TH—oceanic tholeiitic; VAB—volcanic arcs basalts; IAT— island arc tholeiitic; CAB—calk-alkaline basalts; SHO—shoshonitic; TR—transitions between ALK and TH.

Thus, the formation of the dikes in the junction of the Tatarka-Ishimba and Yenisei sutures of the South Yenisei Ridge likely took place during the entire Ediacaran in a transform margin setting due

to oblique subduction in the late Cryogenian [18,21]. Studies of the particularities of magmatism in this region thus help to hypothesize a unified geodynamic model (Figure 11) for the southwestern margin of Siberia during the Ediacaran. The emplacement of supra-subductional island arc complexes in the Cryogenian formed by oblique subduction was followed by magmatism caused by strike slips between plates and the transition of the continental margin into a transform one, which was mainly manifested by widespread dike complexes of diverse composition (Figure 11).

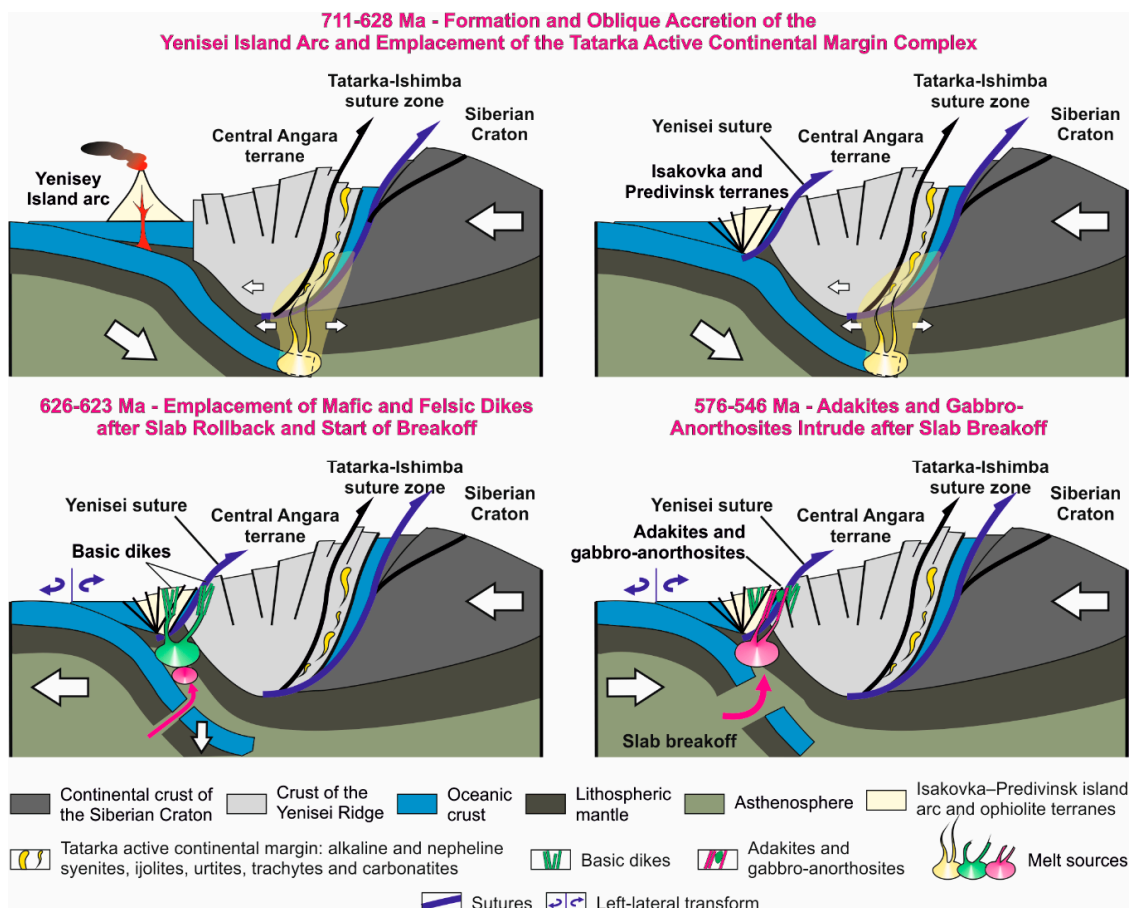


Figure 11. Geodynamic model for the Cryogenian-Ediacaran development stage of the southwestern Siberian active continental margin in the Yenisei Ridge.

6. Conclusions

This paper presents new data for the early Ediacaran stage of magmatism in the evolution of the western margin of the Siberian Craton on the example of a dike complex on the Yenisei Ridge. The discussions on the formation conditions of these rocks are ongoing in the literature. We hope that these data and our conclusions can lead to progress in understanding the tectonomagmatic evolution of the western margin of the Siberian Craton in the Ediacaran:

Within fragments of the structures of the southwestern margin of the Siberia craton, dikes of various igneous rocks have been identified. The mafic dike rocks formed from enriched mantle sources of OIB and E-MORB types. During the evolution of the mantle-sourced mafic melts there was assimilation of crustal material, which led to the formation of Th-enriched dikes of intermediate composition and K- and Rb-enriched felsic rocks.

U-Pb (SHRIMP-II SIMS) data for zircons from picrodolerites, quartz diorites, and leucocratic granites show that these dikes were emplaced between 626 and 623 Ma, which indicates magmatic events in a narrow time interval in the early Ediacaran.

Our new data for igneous rocks of the early Ediacaran of the Yenisei Ridge allow us to propose a geodynamic model for the Cryogenian–Ediacaran development stage of the whole southwestern active continental margin of the Siberian Craton (Figure 11). The model shows that in this early Ediacaran stage, subduction was interrupted, slab rollback took place, and the slab began to break off. This created conditions for the introduction of enriched mantle melts that contributed to the formation of the studied mafic rocks. The active continental margin that was formed as a result of oblique subduction subsequently underwent strike-slip displacements between plates and transitioned to a transform stage, which created conditions for the formation of an adakite-gabbro-anorthosite association.

Supplementary Materials: The following are available online at <http://www.mdpi.com/2075-163X/10/6/565/s1>. Table S1: Chemical compositions of feldspars from the mafic-intermediate-felsic rocks; Table S2: Chemical compositions of clinopyroxenes from the mafic-intermediate rocks; Table S3: Chemical compositions of biotite group minerals from the mafic-intermediate-felsic rocks; Table S4: Chemical compositions of amphiboles from quartz diorite (sample A09-11) (Reference [49] is cited in supplementary materials); Table S5: Chemical compositions of muscovite group minerals from leucocratic granites (sample M08-03).

Author Contributions: Conceptualization, A.V. and V.A.V.; methodology, A.V. and V.A.V.; validation, N.M. and A.V.; formal analysis, P.K. and N.M.; investigation, A.V., V.A.V., N.M., Z.-X.L., I.R., and D.V.M.; resources, A.V., V.A.V., D.V.M., Z.-X.L.; data curation, P.K. and E.B.; writing—original draft preparation, A.V. and N.M.; writing—review and editing, V.A.V.; visualization, N.M., P.K., and E.B.; supervision, V.A.V.; project administration, A.V. and V.A.V.; funding acquisition, V.A.V. All authors have read and agreed to the published version of the manuscript.

Funding: This research has received funding from the Russian Foundation for Basic Research, grants number 18-05-00854, 18-05-00234, 18-35-00556, and 20-05-00360.

Acknowledgments: The authors offer thanks to Alexander Larionov (Centre of Isotopic Research, VSEGEI, Saint Petersburg, Russia) for helping with U-Pb SHRIMP investigations, as well as to Aleksandr Nepomnyashchikh, and Olga Zarubina (A.P. Vinogradov Institute of Geochemistry SB RAS, Irkutsk, Russia) for carrying out ICP-MS analyzes and to Dmitry A. Zedgenizov (V.S. Sobolev Institute of Geology and Mineralogy SB RAS, Novosibirsk, Russia) for help in organizing the mineralogical studies. We also thank the two anonymous reviewers for very useful comments.

Conflicts of Interest: The authors declare no conflicts of interest. The funders had no role in the design of the study; in the collection, analyses, or interpretation of data; in the writing of the manuscript, or in the decision to publish the results.

References

1. Khomentovsky, V.V.; Shenfil', V.Y.; Yakshin, M.S.; Butakov, E.P. *Key Sections of Precambrian and Lower Cambrian Deposits in the Siberian Platform*; Nauka: Moscow, Russia, 1972; 356p. (In Russian)
2. Berzin, N.A.; Dobretsov, N.L. Geodynamic evolution of Southern Siberia in Late Precambrian-Early Paleozoic time. In *Reconstruction of the Paleasian Ocean*; Coleman, R.G., Ed.; VSP International Sciences Publishers: Utrecht, The Netherlands, 1993; pp. 45–62.
3. Khain, V.E.; Gusev, G.S.; Khain, E.V.; Vernikovskiy, V.A.; Volobuyev, M.I. Circum-Siberian Neoproterozoic ophiolite belt. *Ofoliti* **1997**, *21*, 195–200.
4. Vernikovskiy, V.A.; Vernikovskaya, A.E.; Kotov, A.B.; Sal'nikova, E.B.; Kovach, V.P. Neoproterozoic accretionary and collisional events on the western margin of the Siberian Craton: New geological and geochronological evidence from the Yenisey Ridge. *Tectonophysics* **2003**, *375*, 147–168. [[CrossRef](#)]
5. Sovetov, J.K.; Kulikova, A.E.; Medvedev, M.N. Sedimentary basins in the southwestern Siberian craton: Late Neoproterozoic–Early Cambrian rifting and collisional events. *Geol. Soc. Am. Spec. Pap.* **2007**, *423*, 549–578. [[CrossRef](#)]
6. Vernikovskiy, V.A.; Metelkin, D.V.; Vernikovskaya, A.E.; Matushkin, N.Y.; Kazansky, A.Y.; Kadilnikov, P.I.; Romanova, I.V.; Wingate, M.T.D.; Larionov, A.N.; Rodionov, N.V. Neoproterozoic tectonic structure of the Yenisei Ridge and formation of the western margin of the Siberian Craton based on new geological, paleomagnetic, and geochronological data. *Rus. Geol. Geophys.* **2016**, *57*, 47–68. [[CrossRef](#)]
7. Filippov, Y.F. The Fore-Yenisei sedimentary basin: Seismic-geological model and geodynamic history. *Rus. Geol. Geophys.* **2017**, *58*, 371–383. [[CrossRef](#)]

8. Vernikovskaya, A.E.; Vernikovskiy, V.A.; Sal'nikova, E.B.; Datsenko, V.M.; Kotov, A.B.; Kovach, V.P.; Travin, A.V.; Yakovleva, S.Z. Yeruda and Chirimba granitoids (Yenisei Ridge) as indicators of Neoproterozoic collisions. *Geol. I Geofiz.* **2002**, *43*, 259–272.
9. Vernikovskaya, A.E.; Vernikovskiy, V.A.; Sal'nikova, E.B.; Kotov, A.B.; Kovach, V.P.; Travin, A.V.; Wingate, M.T.D. A-type leucogranite magmatism in the evolution of continental crust on the western margin of the Siberian Craton. *Rus. Geol. Geophys.* **2007**, *48*, 3–16. [[CrossRef](#)]
10. Vernikovskiy, V.A.; Vernikovskaya, A.E.; Sal'nikova, E.B.; Berezhnaya, N.G.; Larionov, A.N.; Kotov, A.B.; Kovach, V.P.; Vernikovskaya, I.V.; Matushkin, N.Y.; Yasenev, A.M. Late Riphean alkaline magmatism in the western framework of the Siberian Craton: A result of continental rifting or accretionary events? *Dokl. Earth Sci.* **2008**, *419*, 226–230. [[CrossRef](#)]
11. Vernikovskiy, V.A.; Vernikovskaya, A.E.; Sal'nikova, E.B.; Kotov, A.B.; Chernykh, A.I.; Kovach, V.P.; Berezhnaya, N.G.; Yakovleva, S.Z. New U–Pb data on the formation of the Predivinsk paleoisland-arc complex (Yenisei Ridge). *Geol. I Geofiz.* **1999**, *2*, 255–259.
12. Vernikovskiy, V.A.; Vernikovskaya, A.E.; Chernykh, A.I.; Sal'nikova, E.B.; Kotov, A.B.; Kovach, V.P.; Yakovleva, S.Z.; Fedoseenko, A.M. Porozhnaya granitoids of the Enisei ophiolite belt: Indicators of Neoproterozoic events on the Enisei Ridge. *Dokl. Earth Sci.* **2001**, *381A*, 1043–1046.
13. Kuzmichev, A.B.; Paderin, I.P.; Antonov, A.V. Late Riphean Borisikha ophiolite (Yenisei Ridge): U–Pb zircon age and tectonic setting. *Rus. Geol. Geophys.* **2008**, *49*, 883–893. [[CrossRef](#)]
14. Vernikovskaya, A.E.; Vernikovskiy, V.A.; Matushkin, N.Y.; Kadil'nikov, P.I.; Romanova, I.V.; Larionov, A.N. Late Neoproterozoic adakites of the Yenisei Ridge (Central Siberia): Petrogenesis, geodynamics, and U/Pb age. *Rus. Geol. Geophys.* **2017**, *58*, 1154–1170. [[CrossRef](#)]
15. Gladkochub, D.P.; Wingate, M.T.D.; Pisarevsky, S.A.; Donskaya, T.V.; Mazukabzov, A.M.; Ponomarchuk, V.A.; Stanevich, A.M. Mafic intrusions in southwestern Siberia and implications for a Neoproterozoic connection with Laurentia. *Prec. Res.* **2006**, *147*, 260–278. [[CrossRef](#)]
16. Nozhkin, A.D.; Turkina, O.M.; Bayanova, T.B.; Berezhnaya, N.G.; Larionov, A.N.; Postnikov, A.A.; Travin, A.V.; Ernst, R.E. Neoproterozoic rift and within-plate magmatism in the Yenisei Ridge: Implications for the breakup of Rodinia. *Rus. Geol. Geophys.* **2008**, *49*, 503–519. [[CrossRef](#)]
17. Vernikovskiy, V.A.; Vernikovskaya, A.E.; Pease, V.L.; Gee, D.G. Neoproterozoic Orogeny along the margins of Siberia. In *The Neoproterozoic Timanide Orogen of Eastern Baltica*; Gee, D.G., Pease, V., Eds.; Geological Society, London, Memoirs: London, UK, 2004; Volume 30, pp. 233–247. [[CrossRef](#)]
18. Vernikovskiy, V.A.; Vernikovskaya, A.E. Tectonics and evolution of granitoid magmatism in the Yenisei Ridge. *Rus. Geol. Geophys.* **2006**, *47*, 35–52.
19. Metelkin, D.V.; Vernikovskiy, V.A.; Kazansky, A.Y. Neoproterozoic evolution of Rodinia: Constraints from new paleomagnetic data on the western margin of the Siberian craton. *Rus. Geol. Geophys.* **2007**, *48*, 32–45. [[CrossRef](#)]
20. Metelkin, D.V.; Vernikovskiy, V.A.; Matushkin, N.Y. Arctida between Rodinia and Pangea. *Prec. Res.* **2015**, *259*, 114–129. [[CrossRef](#)]
21. Vernikovskaya, A.E.; Datsenko, V.M.; Vernikovskiy, V.A.; Matushkin, N.Y.; Laevsky, Y.M.; Romanova, I.V.; Travin, A.V.; Voronin, K.V.; Lepekhina, E.N. Magmatism evolution and carbonatite-granite association in the Neoproterozoic active continental margin of the Siberian Craton: Thermochronological reconstructions. *Dokl. Earth Sci.* **2013**, *448*, 161–167. [[CrossRef](#)]
22. Kachevsky, L.K.; Kachevskaya, G.I.; Grabovskaya, Z.M. *Geological Map of the Yenisei Ridge, Scale 1:500,000*; Krasnoyarskgeolsyemka: Krasnoyarsk, Russia, 1998. (In Russian)
23. Vernikovskaya, A.E.; Vernikovskiy, V.A.; Sal'nikova, E.B.; Kotov, A.B.; Kovach, V.P.; Travin, A.V.; Palessky, S.V.; Yakovleva, S.Z.; Yasenev, A.M.; Fedoseenko, A.M. Neoproterozoic postcollisional granitoids of the Glushikha complex, Yenisei Ridge. *Petrology* **2003**, *11*, 53–67.
24. Vernikovskiy, V.A.; Kazansky, A.Y.; Matushkin, N.Y.; Metelkin, D.V.; Sovetov, J.K. The geodynamic evolution of the folded framing and the western margin of the Siberian Craton in the Neoproterozoic: Geological, structural, sedimentological, geochronological, and paleomagnetic data. *Rus. Geol. Geophys.* **2009**, *50*, 380–393. [[CrossRef](#)]
25. Vernikovskaya, A.E.; Vernikovskiy, V.A.; Sal'nikova, E.B.; Datsenko, V.M.; Kotov, A.B.; Kovach, V.P. A Neoproterozoic anorogenic event in the Yenisei Ridge: New geochemical and isotopic-geochronological data. *Dokl. Earth Sci.* **2005**, *403*, 833–837.

26. Romanova, I.V.; Vernikovskaya, A.E.; Vernikovskiy, V.A.; Matushkin, N.Y.; Larionov, A.N. Neoproterozoic alkaline magmatism and associated igneous rocks in the western framing of the Siberian Craton: Petrography, geochemistry, and geochronology. *Rus. Geol. Geophys.* **2012**, *53*, 1176–1196. [CrossRef]
27. Amosova, A.A.; Panteeva, S.V.; Tatarinov, V.V.; Chubarov, V.M.; Finkelshtein, A.L. X-ray fluorescent determination of the main rock-forming elements from 50 and 110 mg samples. *Anal. I Kontrol Anal. Control* **2015**, *19*, 130–138. [CrossRef]
28. Smirnova, E.V.; Flem, B.; Anchutina, E.A.; Mysovskaya, I.N.; Lozhkin, V.I.; Petrov, L.L. Determination of REE, Y, Nb, Zr, Hf, Ta, Th and U in geological reference materials LSHC-1 and Amf-1 by solution and laser ablation ICP-MS. *Geostand. Geoanalytic. Res.* **2010**, *34*, 49–65. [CrossRef]
29. Evensen, N.M.; Hamilton, P.S.; O’Nions, R.K. Rare-earth abundances in chondritic meteorites. *Geochim. Cosmochim. Acta* **1978**, *41*, 1199–1212. [CrossRef]
30. McDonough, W.F.; Sun, S.-S. The composition of the Earth. *Chem. Geol.* **1995**, *120*, 223–253. [CrossRef]
31. Black, L.P.; Kamo, S.L.; Allen, C.M.; Aleinikoff, J.N.; Davis, D.W.; Korsch, R.J.; Foudoulis, C. TEMORA 1: A new zircon standard for Phanerozoic U-Pb geochronology. *Chem. Geol.* **2003**, *200*, 155–170. [CrossRef]
32. Wiedenbeck, M.; Allé, P.; Corfu, F.; Griffin, W.L.; Meier, M.; Oberli, F.; von Quadt, A.; Roddick, J.C.; Spiegel, W. Three natural zircon standards for U-Th-Pb, Lu-Hf, trace element and REE analyses. *Geostand. Newslet.* **1995**, *11*, 1–23. [CrossRef]
33. Larionov, A.N.; Andreichev, V.A.; Gee, D.G. The Vendian alkaline igneous suite of northern Timan: Ion microprobe U–Pb zircon ages of gabbros and syenite. In *The Neoproterozoic Timanide Orogen of Eastern Baltica*, 1st ed.; Gee, D.G., Pease, V.L., Eds.; Geology. Society, London, Memoirs: London, UK, 2004; Volume 30, pp. 69–74. [CrossRef]
34. Ludwig, K.R. *SQUID 1.12 A User’s Manual. A Geochronological Toolkit for Microsoft Excel*, 1st ed.; Berkeley Geochronology Center Special Publication: Berkeley, CA, USA, 2005; 22p, Available online: http://bgc.org/isoplot_etc/squid/SQUID2_5Manual.pdf (accessed on 21 June 2020).
35. Ludwig, K.R. *User’s Manual for ISOPLOT/Ex 3.22. A Geochronological Toolkit for Microsoft Excel*, 3rd ed.; Berkeley Geochronology Center Special Publication: Berkeley, CA, USA, 2005; 71p, Available online: http://www.bgc.org/isoplot_etc/isoplot/Isoplot3_75-4_15manual.pdf (accessed on 21 June 2020).
36. Stacey, J.S.; Kramers, J.D. Approximation of terrestrial lead isotope evolution by a two-stage model. *Earth Planet. Sci. Lett.* **1975**, *21*, 207–221. [CrossRef]
37. Whitney, D.L.; Evans, B.P. Abbreviations for names of rock-forming minerals. *Am. Mineral.* **2010**, *91*, 185–187. [CrossRef]
38. Deer, W.A.; Howie, R.A.; Zussman, J. *An Introduction to the Rock-Forming Minerals*, 2nd ed.; Longman Scientific & Technical: London, UK, 1992; 696p.
39. Morimoto, N. Nomenclature of Pyroxenes. *Mineral. Petrol.* **1988**, *39*, 55–76. [CrossRef]
40. Nwe, Y.Y. Electron-probe studies of the earlier pyroxenes and olivines from the Skaergaard Intrusion, East Greenland. *Contrib. Mineral. Petrol.* **1976**, *55*, 105–126. [CrossRef]
41. Gutiérrez, F.; Gioncada, A.; González Ferran, O.; Lahsen, A.; Mazzuoli, R. The Hudson Volcano and surrounding monogenetic centres (Chilean Patagonia): An example of volcanism associated with ridge–trench collision environment. *J. Volcanol. Geotherm. Res.* **2005**, *145*, 207–233. [CrossRef]
42. Parlak, O.; Karaoglan, F.; Rizaoglu, T.; Nurlu, N.; Bagci, U.; Höck, V.; Öztüfekci Önal, A.; Kürüm, S.; Topak, Y. Petrology of the Ispendere (Malatya) ophiolite from the Southeast Anatolia: Implications for the late Mesozoic evolution of the southern Neotethyan Ocean. *Geol. Soc. Lond. Spec. Publ.* **2012**, *372*, 219. [CrossRef]
43. Volynets, O.N. Geochemical types, petrology and genesis of late Cenozoic volcanic rocks from the Kurile-Kamchatka island-arc system. *Inter. Geol. Rev.* **1991**, *36*, 373–405. [CrossRef]
44. Le Maitre, R.W. *A Classification of Igneous Rocks and Glossary of Terms*; Blackwell Scientific Publications: Oxford, UK, 1989; 193p.
45. Le Bas, M.J. IUGS reclassification of the high-Mg and picritic volcanic rocks. *J. Petrol.* **2000**, *41*, 1467–1470. [CrossRef]
46. Miyashiro, A. Volcanic rock series in island arcs and active continental margins. *Am. J. Sci.* **1974**, *271*, 321–355. [CrossRef]
47. Pearce, J.A. Geochemical fingerprinting of oceanic basalts with applications to ophiolite classification and the search for Archean oceanic crust. *Lithos* **2008**, *100*, 14–48. [CrossRef]

48. Pearce, J.A. Trace element characteristics of lavas from destructive plate boundaries. In *Andesites: Orogenic Andesites and Related Rocks*; Wyman, D.A., Ed.; John Wiley & Sons, Ltd.: Chichester, UK, 1982; pp. 525–548.
49. Leake, B.E.; Woolley, A.R.; Arps, C.E.S.; Birch, W.D.; Gilbert, M.C.; Grice, J.D.; Hawthorne, C.; Kato, A.; Kisch, H.J.; Krivovichev, V.G.; et al. Nomenclature of amphiboles: Report of the Subcommittee on Amphiboles of the International Mineralogical Association, Commission on New Minerals and Mineral Names. *Mineral. Mag.* **1997**, *61*, 295–310. [[CrossRef](#)]



© 2020 by the authors. Licensee MDPI, Basel, Switzerland. This article is an open access article distributed under the terms and conditions of the Creative Commons Attribution (CC BY) license (<http://creativecommons.org/licenses/by/4.0/>).